

# Chemical Tomography in a Fresh Wildland Fire Plume: A Large Eddy Simulation (LES) Study

### Key Points:

- Photochemistry is active at the edges of thick fire plumes, while dark chemistry is present in the lower part and below thick plumes
- Hydroxyl radicals formed from nitrous acid drive the plume oxidation; nitrous acid may be produced on aerosols
- Model resolution affects chemistry; sufficiently high spatial resolution is needed to capture the impacts of wildfires on air quality

### Supporting Information:

Supporting Information may be found in the online version of this article.

### Correspondence to:

S. Wang,  
[siyuan.wang@noaa.gov](mailto:siyuan.wang@noaa.gov)
























### Citation:

Wang, S., Coggon, M. M., Gkatzelis, G. I., Warneke, C., Bourgeois, I., Ryerson, T., et al. (2021). Chemical tomography in a fresh wildland fire plume: A large eddy simulation (LES) study. *Journal of Geophysical Research: Atmospheres*, 126, e2021JD035203. <https://doi.org/10.1029/2021JD035203>

Received 5 MAY 2021  
 Accepted 2 SEP 2021

### Author Contributions:

**Conceptualization:** Siyuan Wang  
**Formal analysis:** Siyuan Wang  
**Investigation:** Siyuan Wang  
**Methodology:** Siyuan Wang  
**Software:** Siyuan Wang  
**Supervision:** Siyuan Wang  
**Validation:** Siyuan Wang  
**Visualization:** Siyuan Wang  
**Writing – original draft:** Siyuan Wang  
**Writing – review & editing:** Siyuan Wang

Siyuan Wang<sup>1,2,3</sup> , Matthew M. Coggon<sup>1,2</sup> , Georgios I. Gkatzelis<sup>1,2,4</sup> , Carsten Warneke<sup>1,2</sup> , Ilann Bourgeois<sup>1,2</sup> , Thomas Ryerson<sup>2</sup> , Jeff Peischl<sup>1,2</sup> , Patrick R. Veres<sup>2</sup> , J. Andrew Neuman<sup>1,2</sup> , Johnathan Hair<sup>5</sup> , Taylor Shingler<sup>5</sup>, Marta Fenn<sup>5,6</sup> , Glenn Diskin<sup>5</sup> , L. Greg Huey<sup>7</sup> , Young Ro Lee<sup>7</sup>, Eric C. Apel<sup>3</sup> , Rebecca S. Hornbrook<sup>3</sup> , Alan J. Hills<sup>3</sup>, Samuel R. Hall<sup>3</sup> , Kirk Ullmann<sup>3</sup> , Megan M. Bela<sup>1,2</sup> , Michael K. Trainer<sup>1,2</sup> , Rajesh Kumar<sup>8</sup> , John J. Orlando<sup>3</sup> , Frank M. Flocke<sup>3</sup> , and Louisa K. Emmons<sup>3</sup> 

<sup>1</sup>Cooperative Institute for Research in Environmental Sciences (CIRES), University of Colorado, Boulder, CO, USA, <sup>2</sup>National Oceanic and Atmospheric Administration (NOAA), Chemical Sciences Laboratory (CSL), Boulder, CO, USA, <sup>3</sup>National Center for Atmospheric Research (NCAR), Atmospheric Chemistry Observations and Modeling Laboratory (ACOM), Boulder, CO, USA, <sup>4</sup>Now at Institute of Energy and Climate Research, IEK-8: Troposphere, Forschungszentrum Jülich GmbH, Jülich, Germany, <sup>5</sup>National Aeronautics and Space Administration, Langley Research Center, Hampton, VA, USA, <sup>6</sup>Science Systems and Applications, Inc., Hampton, VA, USA, <sup>7</sup>School of Earth and Atmospheric Sciences, Georgia Institute of Technology, Atlanta, GA, USA, <sup>8</sup>National Center for Atmospheric Research (NCAR), Research Applications Laboratory (RAL), Boulder, CO, USA

**Abstract** Wildland fires involve complicated processes that are challenging to represent in chemical transport models. Recent airborne measurements reveal remarkable chemical tomography in fresh wildland fire plumes, which remain yet to be fully explored using models. Here, we present a high-resolution large eddy simulation model coupled to chemistry to study the chemical evolution in fresh wildland fire plume. The model is configured for a large fire heavily sampled during the Fire Influence on Regional to Global Environments and Air Quality field campaign, and a variety of airborne measurements are used to evaluate the chemical heterogeneity revealed by the model. We show that the model captures the observed cross-transect variations of a number of compounds quite well, including ozone (O<sub>3</sub>), nitrous acid (HONO), and peroxyacetyl nitrate. The combined observational and modeling results suggest that the top and edges of fresh plume drive the photochemistry, while dark chemistry is also present but in the lower part of the plume. The model spatial resolution is shown to be very important as it may shift the chemical regime, leading to biases in O<sub>3</sub> and NO<sub>x</sub> chemistry. Based on findings in this work, we speculate that the impact of small fires on air quality may be largely underestimated in models with coarse spatial resolutions.

**Plain Language Summary** Recent fire seasons in the United States have been record-setting for many states. Several large wildfires raged across the entire west coast and lofted smoke plumes spread to the majority of the continental U.S. From a scientific perspective, wildland fires are fascinating due to their complexity. Fires emit heat, creating a plume of hot and turbulent air. The fire plume also contains many gases and aerosol particles produced from the burning and baking of a variety of fuels on the ground (trees, grasses, leaf litter and other fallen debris, etc.). Many of these gases and aerosol particles can impact climate, air quality, and human health. For this reason, most modern air quality and climate models now consider wildland fires. However, wildland fires are fundamentally challenging for these models, because many fine-scale and large-scale processes are entangled at the same time. In this work, we use a high-resolution turbulence-resolving numerical model to study the fine details in a wildland fire plume, with implications for large-scale air quality and climate models.

## 1. Introduction

Wildland fires are a natural phenomenon and an important component of the global ecosystem. Although the global trends of wildland fires remain a subject of debate (Doerr & Santín, 2016), the projected burned area and the fire season length are expected to increase in the 21st century, especially in the Northern Hemisphere (Doerr & Santín, 2016; Flannigan et al., 2013). In the United States, wildland fires are a growing

concern. Records have shown that large wildfire activity in the United States increased suddenly in the mid-1980s, with higher large-fire frequency, longer wildfire durations, and longer wildfire seasons (Westerling et al., 2006), largely driven by human-caused climate change (Abatzoglou & Williams, 2016).

Wildland fires often pose considerable risks to human health and property, with major impacts on air quality and the climate system. A 2010 survey showed that 32% of the U.S. population reside in “wildland–urban interface areas,” which are defined as areas where structures and other human development meet or intermingle with undeveloped wildland and where wildfires have their greatest impacts on people (Martinuzzi et al., 2015). Wildland fires emit a wide range of pollutants and greenhouse gases, such as particulate matter, carbon monoxide (CO), carbon dioxide (CO<sub>2</sub>), volatile organic compounds (VOCs), and reactive nitrogen species (Liu et al., 2017), many of which produce secondary pollutants such as ozone (O<sub>3</sub>) and secondary organic aerosols in the atmosphere (Hodshire, Akherati, et al., 2019; Hodshire, Bian, et al., 2019; Jaffe et al., 2020; Lu et al., 2016; Palm et al., 2020). Growing evidence indicates that wildfire smoke exposure is associated with respiratory morbidity and potentially cardiovascular morbidity as well (Reid et al., 2016). Efforts to improve air quality in the United States show some promising trends as evidenced from improvements in fine particulate matter pollution in the majority of the United States over the past several decades, except in the wildfire-prone regions where air quality has been worsening due to wildfire events (David et al., 2021; Jaffe et al., 2020; McClure & Jaffe, 2018). Given the broad impacts they have on the atmosphere and the climate system, wildland fires are a vital component in most modern chemical transport models and climate models.

The scope of wildland fires ranges from microscale to mesoscale, with influence from both microphysics and chemistry. Wildland fires also involve complicated feedback mechanisms, for example, the fire source and plume alter the flow field and the radiation in the atmosphere; in turn, the meteorology, terrain, and the fuels also affect the fire behavior. As a result, wildland fires are challenging to model. State-of-the-art fire models have been developed to explicitly solve the two-way coupling between weather and fire behavior (Coen, 2013; Mandel et al., 2011). However, models with realistic representations of the two-way coupling with the land/fuel models and the fire-weather interactions are often highly complex and rather computationally demanding, even more so if coupled with chemistry. Most air quality and climate models are not designed to accommodate such complexity. Because of the computational concerns, many air quality/climate models are operated at coarse spatial resolutions and with longer integration time steps. As a result, many key physical and chemical processes (e.g., heat release and plume rise) cannot be explicitly modeled, and hence rely on subgrid parameterizations. This presents a gap between “what is happening” and “what is coded in air quality/climate models.”

Another gap emerges when studying wildland fires using observations. A number of previous field campaigns have revealed remarkable insights into the physical and chemical processes in wildland fire plumes. For logistic and safety reasons, the early stage of the plume (e.g., first hour or younger) remains poorly sampled. Controlled laboratory experiments enable detailed characterizations of the fuel and the initial smoke (e.g., Hodshire, Bian, et al., 2019; Roberts et al., 2020); however, these laboratory studies also only provide limited information on the chemical evolution in the early stages of a wildfire plume. The early stage of the fire plume (e.g., first hour or so) often involves plume rise and dilution, as well as rapid changes in microphysical properties (Hodshire, Akherati, et al., 2019; Konovalov et al., 2019; Schwarz et al., 2008). The early stage of fire plumes remains poorly studied and a better understanding is needed.

Numerical models are a valuable tool to understand the chemical evolution in wildland fire plumes. For instance, Lagrangian models have been used to track the plume-scale chemical evolution (e.g., Alvarado & Prinn, 2009; Alvarado et al., 2015; Coggon et al., 2019; Hodshire, Akherati, et al., 2019; Hodshire, Bian, et al., 2019; Mason et al., 2006; Trentmann et al., 2005) and have greatly advanced our understanding of chemical transformation in wildfire plumes. However, such models are not designed to resolve the spatial heterogeneity in wildfire plumes, which may largely drive the variability in observations within wildfire plumes. In light of this, high-resolution Eulerian-type plume models have been used to study the chemical evolution in wildfire plumes (Alvarado et al., 2009; Trentmann, Andreae, et al., 2003; Trentmann, Früh, et al., 2003; Trentmann et al., 2002). In particular, Trentmann, Andreae, et al. (2003) and Trentmann, Früh, et al. (2003) revealed remarkable chemical heterogeneity within the fire plume, with OH radical enhanced in the edges of the plume, and O<sub>3</sub> suppressed in the early stage of the plume but enhanced in the later stage

(Trentmann, Andreae, et al., 2003; Trentmann, Früh, et al., 2003). Similar spatial heterogeneity in OH and O<sub>3</sub> has been inferred for power plant plumes as well (Brock et al., 2002). However, such Eulerian-type plume models are often computationally demanding, posing a limit to the spatial resolution and/or the domain size, both of which affect the capability of capturing turbulent processes (Agee & Gluhovsky, 1999; de Roode et al., 2004). Moreover, the observational data sets available to evaluate the chemical heterogeneity revealed in such Eulerian models were not readily available in previous studies.

The motivation of this work is to use a high-resolution turbulence-resolving model (large eddy simulation, LES) to study the chemical evolution in the early stages of a wildland fire plume and evaluate the results using airborne observations. The LES model within the Weather Research and Forecasting (WRF) package (Moeng et al., 2007) is coupled to a simple yet representative chemical mechanism. The plume dynamics and interactions with the flow field are resolved; the fire source characteristics, terrain, and variations in the meteorology are highly idealized, allowing to focus on the chemical evolution. The modeling experiment in this work is configured for the Williams Flats Fire (47.9392°N, 118.6183°W), a large wildfire ignited on August 2, 2019 in the State of Washington, U.S. This fire was extensively sampled by a number of research aircraft and satellites during the Fire Influence on Regional to Global Environments and Air Quality (FIREX-AQ) field campaign (July–September 2019). FIREX-AQ was a comprehensive airborne mission jointly funded by National Oceanic and Atmospheric Administration (NOAA) and National Aeronautics and Space Administration (NASA), focusing on the trace gases and aerosols emitted from wildfires and their impacts on air quality and climate in the United States. Airborne measurements collected from the NASA DC-8 aircraft are used to evaluate the chemical heterogeneity predicted by the model.

## 2. WRF-LES-Chemistry Model

In this work, the LES model in the WRF package (version 4.0) is run in an idealized configuration, with a domain size of 70 km × 30 km × 6 km. The horizontal grid resolution is 100 m, and the vertical resolution is ~78 m near the surface and up to 138 m near the top of the model. The total number of grid boxes is 126,000,000, and the time step is 1 s. More details of the LES model configuration are provided in the Section S1. This LES model is coupled with a simple yet representative chemical mechanism, consisting of 39 transported tracers and 69 reactions, covering major tropospheric chemical reactions involving key NO<sub>x</sub>/VOC/O<sub>3</sub> chemistry (Table S1). This chemical mechanism is condensed based on the widely used MOZART T1 mechanism in the WRF package (Knote et al., 2014). Photolysis frequencies are calculated using the Fast Tropospheric Ultraviolet-Visible (FTUV) scheme (Tie et al., 2003). Two inert aerosol tracers, black carbon (BC) and organic carbon (OC), are included in this mechanism, to account for the aerosol impacts on radiation and chemistry, via both photolysis frequencies and heterogeneous chemistry. The LES model is initialized using the vertical soundings (potential temperature, water vapor, and wind) and vertical profiles of chemical species from a mesoscale WRF-Chem simulation for the Williams Flats Fire. More details of this mesoscale WRF-Chem simulation are given in Section S2; Figures S1 and S2. The LES model is spun-up for 2 h (from 20:00:00 to 22:00:00 August 3, 2019, all times are in UTC unless otherwise noted; UTC, Coordinated Universal Time) and simulated for three more hours (22:00:00 August 3 2019 to 01:00:00 August 4, 2019). The fire plume in this LES model is driven by surface fluxes of sensible heat and chemicals, characterized based on measurements: the fire size is 0.66 km<sup>2</sup> and the sensible heat flux is 10<sup>4</sup> W/m<sup>2</sup>, both approximated from the GOES-16 fire detection product (Li et al., 2020) for the Williams Flats Fire. The emission fluxes of chemical species are adjusted until a reasonable agreement between the modeling results and the airborne measurements is reached (Section 3). The adjusted emission fluxes are given in Table S2. This LES configuration does not have terrain, posing another limitation to the capability of resolving the observed plume transport and dispersion.

## 3. Airborne Observations Used for Model Evaluation

On August 3, 2019, the DC-8 aircraft sampled the Williams Flats Fire plume in two flight patterns: First, an overpass (bird's eye view, red lines in the left panels of Figure 1) above the plume from 21:45 UTC to 21:59 UTC over the plume provides the structure of the plume along the direction of the spread of the fire plume using the downward-looking NASA Langley Airborne Differential Absorption Lidar (DIAL). Second, the

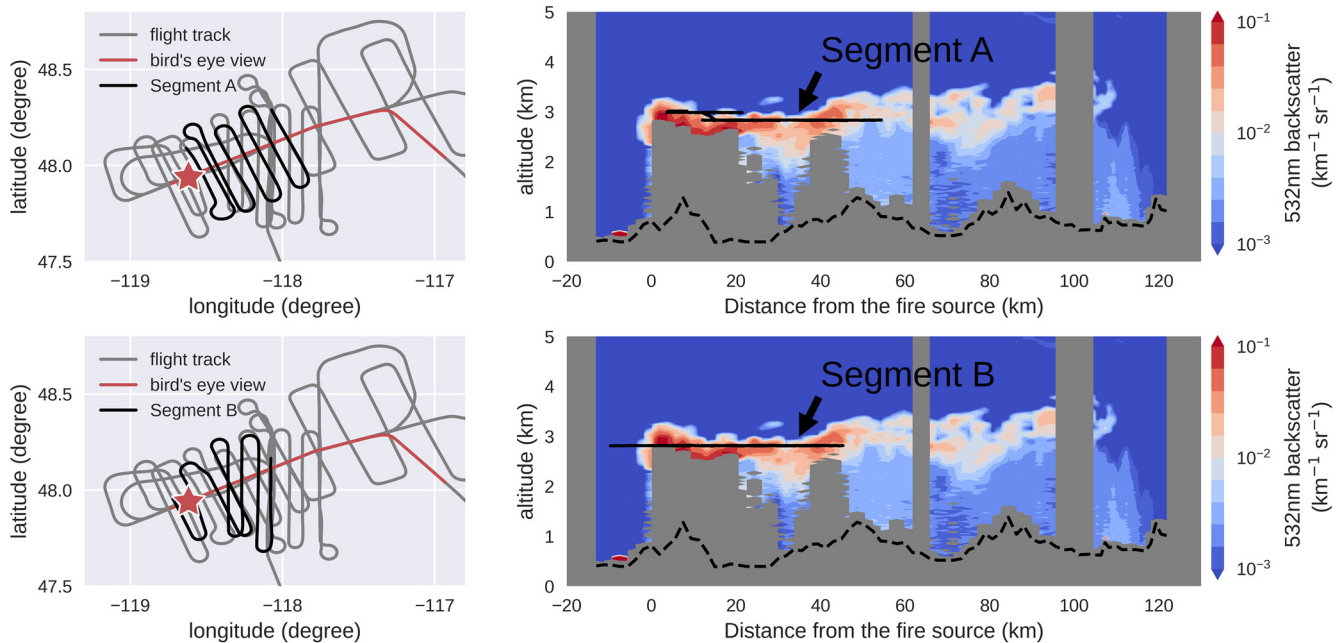


**Figure 1.** (Left) Flight tracks and (right) 532 nm backscatter ratio measured using National Aeronautics and Space Administration (NASA) Differential Absorption Lidar (DIAL). Red stars in the left panel represents the approximate location of the fire source. Gray lines in the left panel shows the entire flight track, while the red lines denote the flight legs when the aircraft was flying above the smoke, producing the “bird’s eye view” that are shown on the right panel. The flight altitudes during Segments A and B (solid black lines in the right panel) are overlaid on top of the “bird’s eye view” curtain in the right panel, but Segments A and B occurred at different times than the “bird’s eye view” flight.

aircraft descended and flew through the plume in a “lawnmower” pattern (i.e., each transect is roughly perpendicular to the direction of plume transport), providing a number of semi-Lagrangian transects (i.e., sampling a plume which evolves in both time and distance while minimizing the distance the plume traveled). The 1-Hz merge data set provided by the NASA Langley Research Center is used in this work, including high time response measurements from a number of instruments, except for the NCAR Trace Organic Gas Analyzer (TOGA-ToF) with a time resolution of  $\sim 105$  s (with a sampling window of  $\sim 32$  s). Table S3 summarizes all measurements used in this work.

The second stage (semi-Lagrangian transects) consists of two segments: Segment A, from 22:20 to 23:15 UTC (August 3, 2019), and Segment B, from 00:30 to 01:24 UTC (August 4, 2019). Segments A and B both sampled the first  $\sim 50$  km of the plume; however, there are two marked differences: (a) Segments A and B were influenced by meteorological differences that result in Segment A representing more diffused/chemically aged plume while Segment B representing fresher plume that had been more recently released into the atmosphere. (b) Based on the combination of remote sensing and in situ measurements, the DC-8 aircraft likely flew through the dense “core” of the plume during Segment B, while Segment A likely skimmed the upper edge of the plume. During Segment B, the sampled plume was rather optically opaque such that the DIAL laser signal was severely attenuated at the center of each transect (Figure 2). Accordingly, the measured photolysis frequencies, such as  $j(\text{NO}_2)$ , were suppressed at the center of each transect (Figure 2).  $\text{O}_3$  was also suppressed at the center of the plume due to the rapid reaction with NO (Figure 2). During Segment A, however, measured CO and  $\text{NO}_x$  levels inside the plume were lower than that during Segment B, and the  $j(\text{NO}_2)$  reduction inside the plume was also weaker than that during Segment B (Figure 2), implying that Segment A perhaps mostly sampled the upper part of the plume, which is optically thinner and with lower levels of primary pollutants. Interestingly,  $\text{O}_3$  during Segment A was always enhanced at the center of each transect (Figure 2), similar to the  $\text{O}_3$  measured when the DC-8 aircraft was entering and leaving the plume in Segment B (i.e., the edges of the plume sampled in Segment B), providing additional evidence that the aircraft sampled the top part of the plume during Segment A. The modified combustion efficiency, defined as  $\Delta\text{CO}_2/(\Delta\text{CO} + \Delta\text{CO}_2)$  (Yokelson et al., 2008), did not vary dramatically between the two segments (both 0.89 and 0.92), implying the average burning condition remained relatively consistent during these



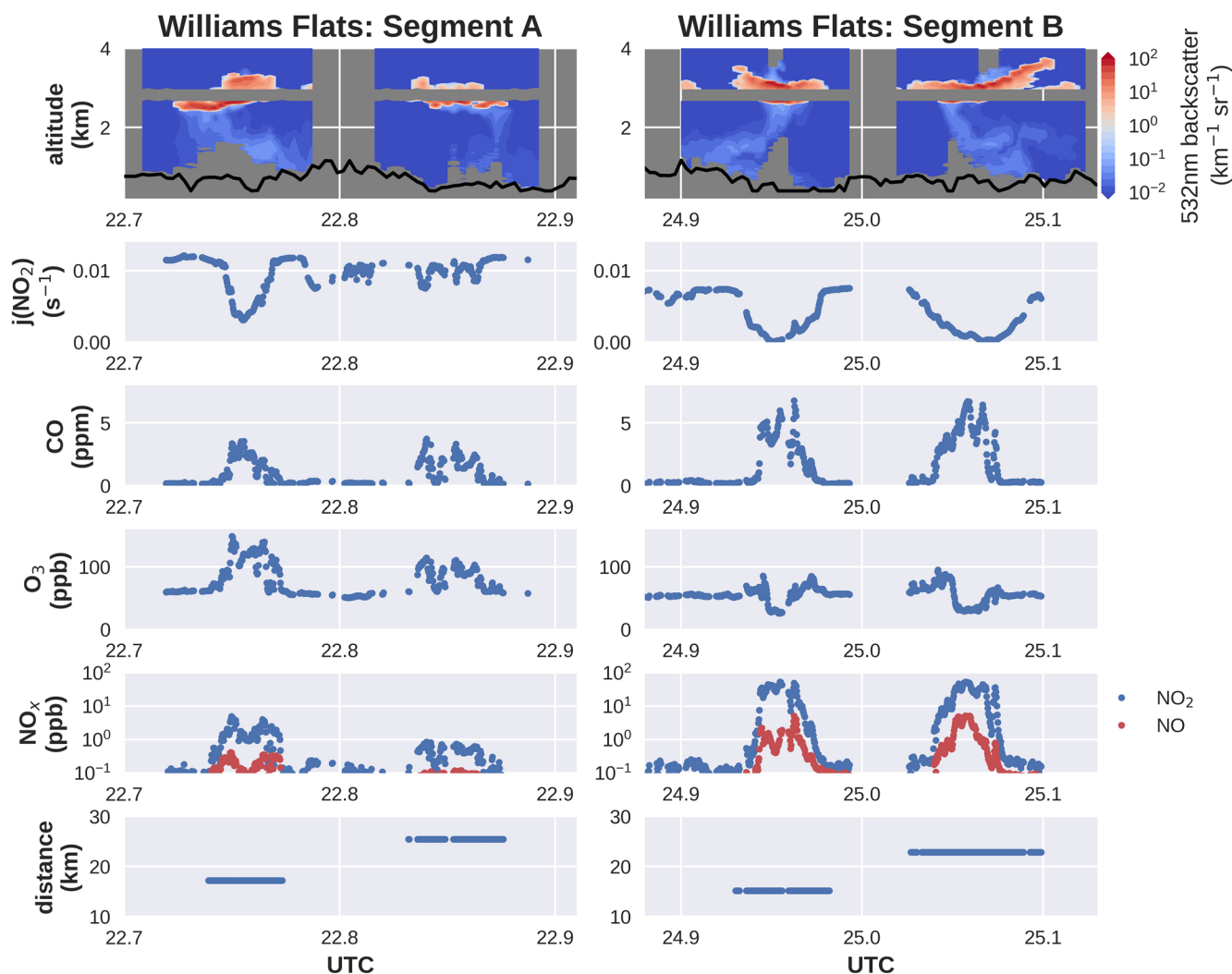


**Figure 2.** Selected airborne measurements collected during the “in-plume” Segments A and B, two transects each. Likely Segment B showed the dark interior of the plume, while Segment A skimmed the top of the plume. The full view of Segments A and B is provided in Figure S3.  $\text{NO}_x$  is plotted on a log scale. Solid black lines in the top panel represent the terrain height. Bottom panels show the distance away from the fire source.

two segments. To summarize, the DC-8 measurements during Segment A may not reflect the center of the plume, and thus Segment B is mainly used for model evaluation.

Figure 3 compares the model chemical species and parameters to the airborne observations collected during Segment B, providing a semiquantitative comparison of the plume chemical evolution as a function of distance in km from the fire source. As shown, the model captures the chemical characteristics within the plume reasonably well, as the modeled plume-wide means of gaseous (CO,  $\text{NO}_x$ , HONO, HCHO,  $\text{O}_3$ , and peroxyacetyl nitrate [PAN]) and aerosol constituents (BC and OC) are both in good agreement with observations, although the observations do show larger variations than the modeled. Modeled maleic anhydride, a major product from furan oxidation, is in good agreement with observations in the first  $\sim 15$  km but shows a factor of  $\sim 2$  discrepancy with observations in the later stage (Figures 3 and 9). This is mainly because the maleic anhydride yield used in this mechanism reflects the upper bound of maleic anhydride production (see note 5 for Table S1). Total VOCs were calculated as the sum of the mixing ratios of ethane, propane, *i*-butane, *n*-butane, *i*-pentane, *n*-pentane, *i*-butene + 1-butene, isoprene, methyl vinyl ketone, methacrolein, benzene, toluene, formaldehyde, acetaldehyde, methanol, ethanol, acrolein, acetone + propanal, furan, 2-methylfuran, 3-methylfuran, furfural, phenol, and styrene, reported from several different instruments on board the DC-8 (Table S3). Notably, the simplified mechanism captures roughly about half of the measured

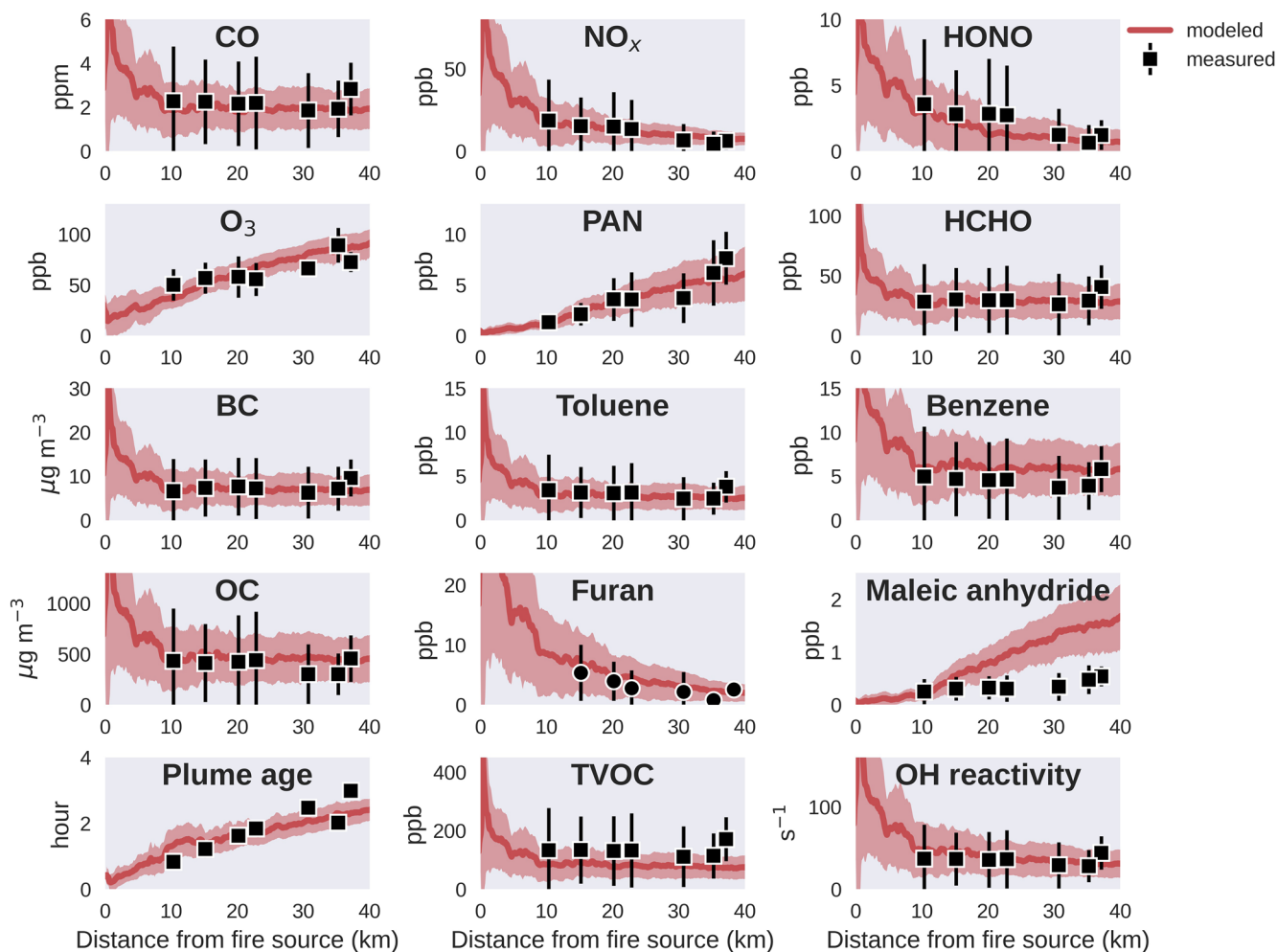


**Figure 3.** Modeled plume-wide averages and standard deviations (red lines and shadings) of selected compounds and parameters, compared to the airborne measurements averages and standard deviations (black symbols and error bars) during each transect during Segment B. The measurements are averaged using the smoke flag provided in the 1-Hz merge, while the modeled plume-wide averages are calculated for each plume cross section. Organic carbon (OC) is calculated from organic aerosol and OA/OC ratio measured using the CU HR-AMS. The measurement-derived plume age is estimated from the measured winds and distance from the fire location (provided in the 1-Hz merge), while the plume age in the model is estimated based on Equation 1. Total measured volatile organic compounds (TVOCs, excluding methane) are listed in the main text and Table S3. Total OH reactivity is calculated for TVOCs as well as CO and methane.

total VOCs, yet the modeled total OH reactivity is comparable to the calculated total OH reactivity based on measurements available (Figure 3).

In the model, two fire tracers are added to track the physical age of any air parcel in the plume: one tracer with 1-h fixed lifetime, and the other inert one with infinite lifetime. The plume physical age (in hours) is given by:

$$\text{Physical age} = -\ln \left[ \frac{\text{Tracer 1}(\tau = 1 \text{ h})}{\text{Tracer 2}(\tau = \infty)} \right], \quad (1)$$

As shown in Figure 3, the modeled physical age also shows good agreement with that estimated using airborne measurements (estimated from measured winds and distance from center of transect to the fire source), implying that the meteorological conditions (especially wind) are decently represented in this simple model configuration. Overall, this figure reveals that the highly simplified model configuration and chemical mechanism captures the major chemical characteristics of the plume. We discuss the detailed plume physics and chemistry in the following sections.

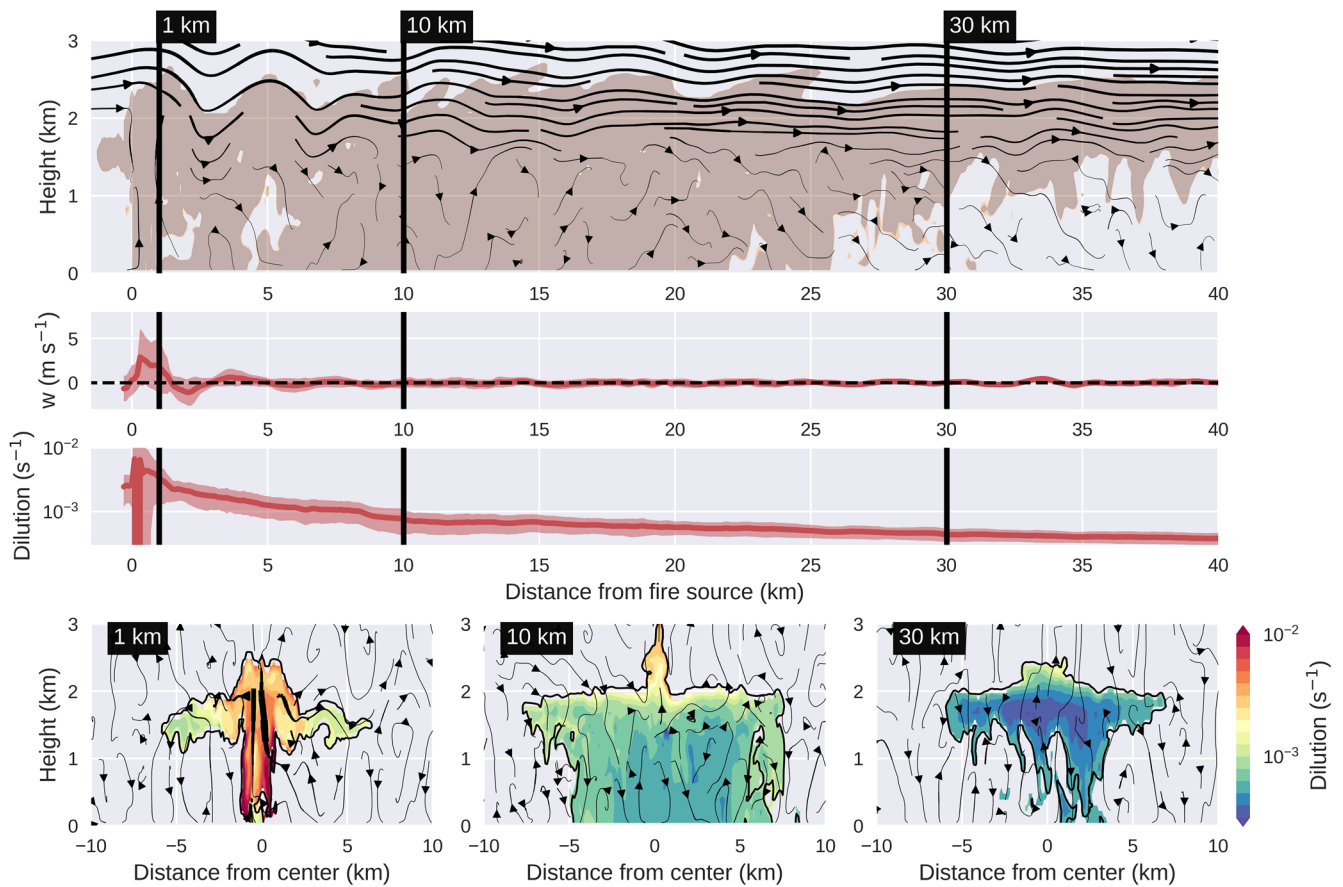


**Figure 4.** (Top) Streamlines at the centerline of the plume (curtain); (middle) plume-wide average updraft speed and dilution rate (shadings: standard deviations); and (bottom) dilution rate cross section at 1, 10, and 30 km from the fire source. The thickness of the streamlines roughly represents the wind speed. The vertical black lines represent the locations of the cross sections. The plume (brown colored area) is defined as CO  $\geq 3E-150$  ppb.

#### 4. Plume Dynamics in the Early Stage of the Plume

The high-resolution LES model resolves the turbulence induced by the fire source and the interactions with the background flow field. Due to the strong heat release from the fire, the plume rapidly rises in the early stage, characterized by high updraft speed in the early stage (modeled mean updraft:  $3 \text{ m s}^{-1}$  in Figure 4; maximum updraft in the model reaches up to  $12 \text{ m s}^{-1}$ ). The strong updraft injects the plume into a lofted layer that is 1.5–2.5 km above the surface, consistent with the DIAL measurements ( $\sim 1.5\text{--}3$  km above ground level, Figures 1 and 2). The rapid updraft at the center of the plume leads to downdraft and hence small circulations near the plume, as indicated by the streamlines in the cross-section plots (Figure 4). The rapid plume rise and the circulations also lead to dilution. In the model, the plume first-order dilution rate can be quantified by tracking the decay of the inert fire tracer:

$$\text{Dilution rate (s}^{-1}\text{)} = \frac{d \ln([\text{Tracer 2}])}{dt} \quad (2)$$

where (Tracer 2) is the concentration of the inert fire tracer and  $t$  is the plume physical age. As shown in Figure 4, the plume dilution rate is on the order of  $0.001 \text{ s}^{-1}$  in the early stage of the plume, which is decreased to and maintained at the order of  $0.0001 \text{ s}^{-1}$  in the late stage of the plume. The plume dilution leads to entrainment of the background air.

Different processes drive the plume dilution. In the uprising stage (e.g., 1 km downwind), the dilution is mostly driven by the circulations induced by the plume rise, therefore faster at the bottom of the plume, where the entrainment flows enter the plume. Later on, the plume rise has ceased (e.g., 10 and 30 km

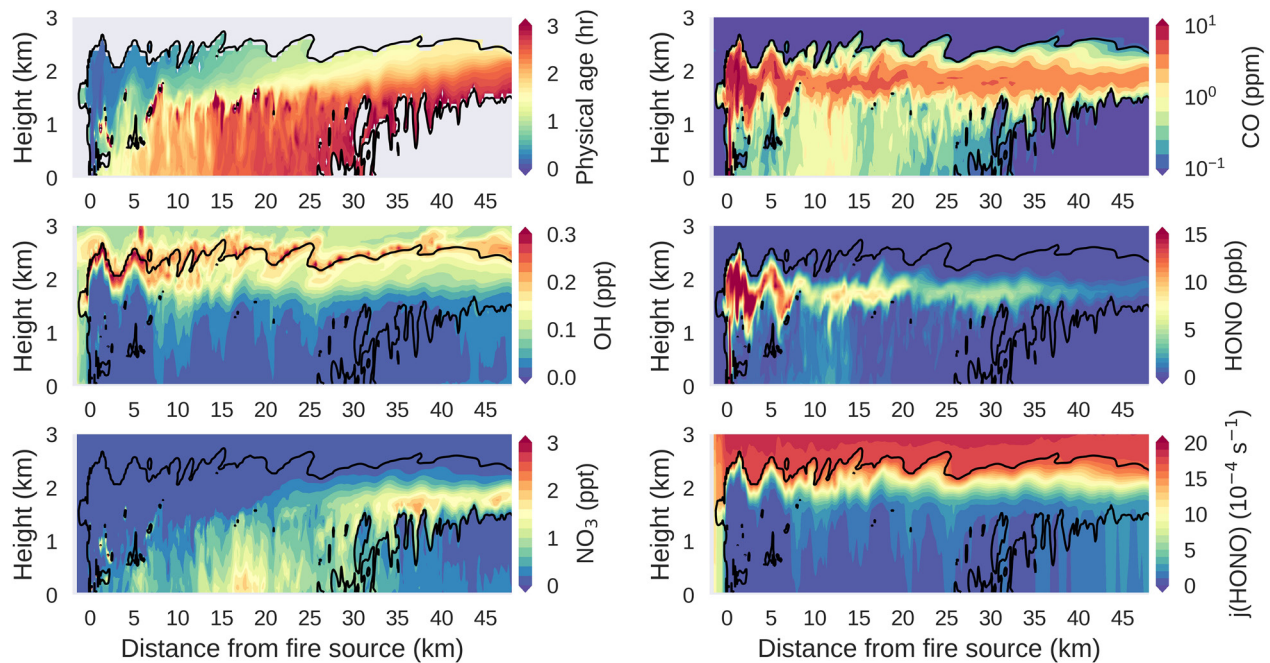


**Figure 5.** Modeled curtains of the plume physical age and mixing ratios of OH, NO<sub>3</sub>, CO, HONO, and the photolysis frequency of HONO. The curtains are at the centerline of the plume. The black lines represent the roughly defined the plume boundary (CO = 150 ppb).

downwind, with mean vertical velocity ( $w$ ) close to zero), the plume-wide mean dilution is nearly an order of magnitude slower than that in the uprising stage and is still faster at the edges of the plume.

Notably, the model predicts the lower part of the plume may be strongly mixed throughout the boundary layer, due to the convective mixing within the boundary layer. As a result, the horizontal dispersion in the lower part of the plume is slower, compared to the upper part (Figure 4). This is typical for daytime wildland fire plumes with low-intermediate plume injection, which is also consistent with the DIAL images that diffused smoke extends from right below the dense smoke all the way to the surface (Figures 1 and 2).

## 5. Physical and Chemical Evolution in the Early Stage of the Plume

The LES configuration coupled with chemistry reveals how the plume evolves over the course of dispersion. Figure 5 briefly shows how the plume ages physically and also provides an overview of the chemical evolution in fresh plume via two important reactive species: OH radicals for photochemistry and NO<sub>3</sub> radicals for dark chemistry. The physical age shows considerable heterogeneity vertically—the lower part of the plume is generally older than the upper part of the plume (Figure 5), which is a combined result of the vertical wind gradient, and enhanced mixing within the boundary layer.

OH radicals are the major driver of atmospheric oxidation. The model predicts very interesting heterogeneity within the fire plume: in the early stage of the plume (first ~8 km or so), OH is severely suppressed in the bulk of the plume but enhanced at the upper most edge of the plume because the rapid HONO photolysis at the upper edge is the dominant OH source (Figure 5; also Section 6.4). This is mainly because the solar radiation is severely attenuated in the plume due to the presence of high levels of aerosols. Further downwind, OH radicals become enhanced in the upper part of the plume (~8–30 km) or even the entire vertical extent of the plume in the later stage (~30+ km, Figure 5). NO<sub>3</sub> radical, a major oxidant in the atmosphere under dark conditions, is also present in the modeled plume at the same time, but only in the lower-most part of the plume and, to a lesser extent, below the thick plume (Figure 5). In particular, the modeled NO<sub>3</sub> mixing ratio reached ~3 ppt in the lower-most part of the plume in the early stage. With the dilution and entrainment, the NO<sub>3</sub> oxidation products in the lower-most part of the plume or below the plume may be mixed into the bulk of the plume. A recent study reported rapid aging of biomass burning aerosols under



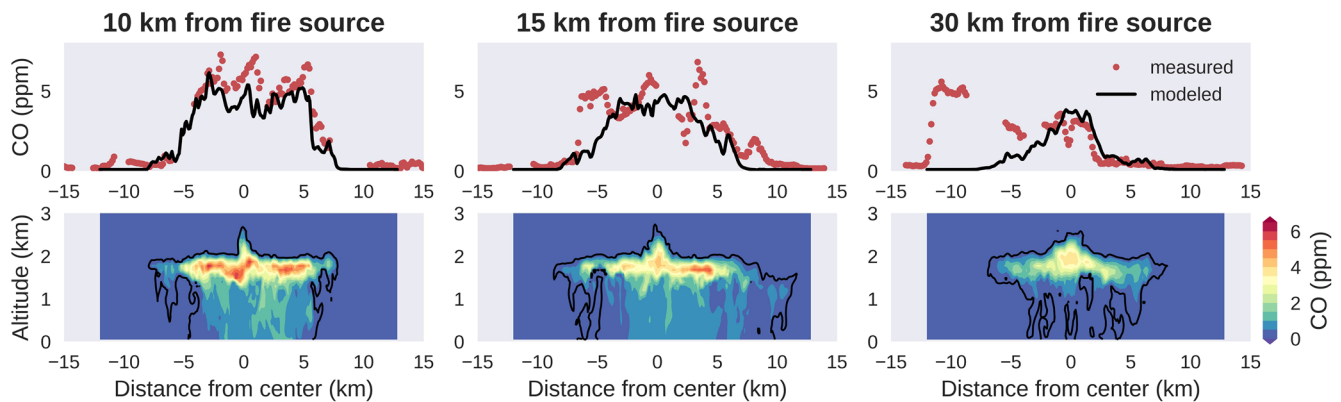


**Figure 6.** Measured CO (top) during Segment B and modeled  $O_3$  cross sections (bottom) at 10, 15, and 30 km downwind of the fire source. Also shown in the top panel are the modeled CO sampled at the same distance from the fire, at  $\sim 2$  km above the model surface.

dark conditions (driven by  $NO_3$  radical), a potential source of organic aerosols that has not been widely considered (Kodros et al., 2020).

## 6. Chemical Tomography in the Plume

In this section, we discuss the modeled chemical tomography inside the plume, focusing on the cross-transect variations of CO,  $O_3$ , PAN, maleic anhydride, and HONO. Again because of the difficulties in providing realistic initial and boundary conditions to the LES model, also the fact that this simplified LES configuration does not consider terrain impact, it is unrealistic to compare the modeling outputs to the DC-8 measurements precisely. Therefore, the modeled fields are not sampled along the flight track. Instead, the comparison is focusing on whether the model can reproduce the broad features in the observations. In this section, several aircraft transects showing distinct cross-transect variations are selected and compared to cross sections of the modeled plume sampled at the same downwind distances at 2 km above the model surface (aircraft altitude:  $\sim 2.8$  km during Segment B, mean terrain height  $0.85 \pm 0.32$  km).

Figure 6 shows the observed cross-transect variability of CO, a major primary emission fire tracer that is long lived with respect to the lifetime of the plume. As shown, the observed CO is generally elevated at the center of the plume, except at 30 km downwind, the observed CO shows two distinct “modes,” possibly due to the influence of very aged/diffused smoke. The modeled cross sections at the same transect distances show very good agreement with observations at 5–15 km downwind. At 30 km downwind, the model is able to capture observations in the center of the transect, but not elevated mixing ratios observed on one edge. Because of the simple model configuration (e.g., short simulation time, small domain, and no smoke in the boundary condition), it is challenging for this model to capture aged/diffused smoke. Overall, Figure 6 demonstrates that the model captures the plume dispersion and transport well in young plumes (up to  $\sim 15$  km from the source).

Similar cross-transect variations for  $NO_x$ , HCHO, BC, and OC are provided in the Supporting Information S1. In general, the model well captures the cross-transect variations of these constituents in the first  $\sim 15$  km (Figures S4–S8), and they are all enhanced inside the plume relative to that at the edges. The model captures the pattern of  $j(\text{HONO})$  but overestimates  $j(\text{HONO})$  inside the plume by  $\sim 20\%$  (relative to the background value, Figure S4). In addition, the in situ measurements show that plume “optical width” (the plume width characterized by the measured  $j$ -values) appears to be wider than the plume “chemical width” (the plume width characterized by the chemical constituents). Although the modeled plume “chemical width” is generally well captured by the model in the first  $\sim 15$  km (Figures 6 and S4–S8), the plume “optical width” is underestimated by the model (Figure S3). The model underestimation of  $j$ -value suppression inside the plume and the underestimation of the plume “optical width” may be due to the 3-D radiation effect (Trentmann, Andreae, et al., 2003; Trentmann, Früh, et al., 2003) that is not captured by FTUV (Tie et al., 2003), although we cannot rule out the possibility of diffused or high level smoke/cloud not captured in the model. Moreover, only BC and OC are considered in this work. Although CU HR-AMS

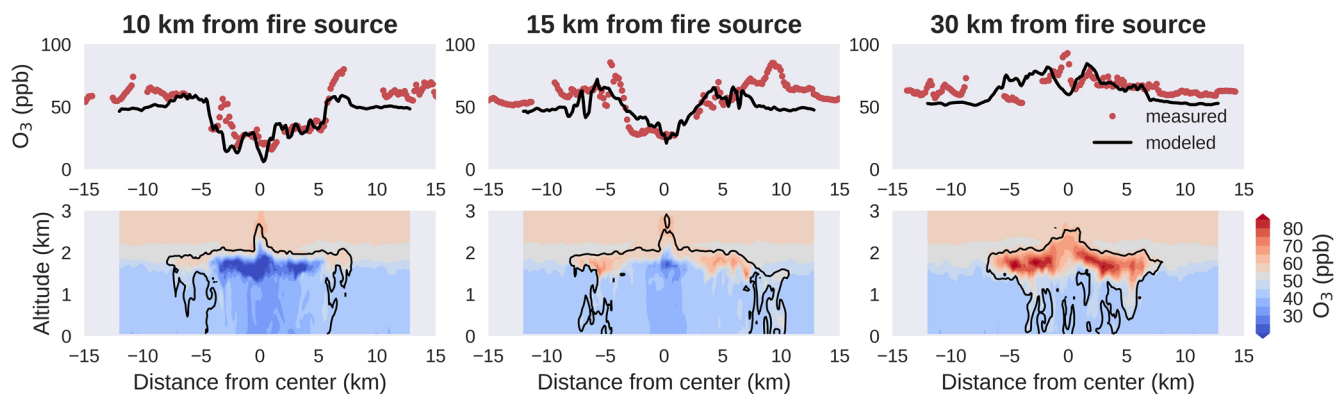


**Figure 7.** Measured  $O_3$  (top) during Segment B and modeled  $O_3$  cross sections (bottom) at 10, 15, and 30 km downwind of the fire source. Also shown in the top panel are the modeled  $O_3$  sampled at the same distance from the fire, at  $\sim 2$  km above the model surface.

measurements suggest that organic aerosols alone accounts for 93% of measured  $PM_{10}$  mass, recent studies found that brown carbon may also contribute to light absorption in biomass burning plumes (e.g., Palm et al., 2020). In summary, primarily fire-emitted long-lived tracers such as CO and BC show Gaussian-like cross-transect profiles. In the next few sections, we will examine a few compounds with drastically different cross-transect profiles.

### 6.1. Cross-Transect Variation of Ozone

As shown in Figure 7,  $O_3$  shows considerable heterogeneity within the modeled plume. In the early stage (10 km downwind), the model predicts that  $O_3$  is suppressed inside the plume (up to 30 ppb lower than the background  $O_3$  at the same height), because of fire-emitted NO. Normally,  $NO_2$  produced from reaction of NO with  $O_3$  would undergo photolysis and produce  $O_3$  back; but  $j(NO_2)$  is strongly suppressed within thick fire plumes, and  $NO_2$  will not photolyze and hence serves as a temporary reservoir for  $O_3$ . The modeled  $O_3$  during this transect compares well to the measurements. At 15 km downwind, measured  $O_3$  is recovered at the center of the transect and is elevated at the edges, and the model shows similar broad features. At 30 km downwind, the measured  $O_3$  is well mixed throughout the plume and is enhanced relative to the background by 10–40 ppb. The model predicts a consistent  $O_3$  trend at 30 km downwind that  $O_3$  is enhanced throughout the plume, compared to the background air.

As discussed in Section 3, Segment B is used to examine the cross-transect variations of  $O_3$ , since the aircraft flew through the core of the plume multiple times during Segment B. However, the edge effect on  $O_3$  is also visible in Segment A, when the aircraft likely sampled the upper edge of the plume. The measured  $O_3$  is enhanced relative to the background in all transects during Segment A (Figure 2) by up to 100 ppb, roughly 2 times greater than the  $O_3$  sampled at the edges of the plume during Segment B. This may indicate possibly stronger  $O_3$  enhancement at the upper edge of the plume than the sides of the plume. The model also shows enhanced  $O_3$  levels at the upper edge of the plume (Figure 7) relative to the sides of the plume, but the magnitude of the  $O_3$  enhancement is again underestimated by the model.

Overall, the model qualitatively captures the observed  $O_3$  variations in these transects but seems to underestimate the  $O_3$  enhancement at the edges. The plume-wide average of  $O_3 + NO_2$  mixing ratio reaches  $\sim 40$  ppb higher than that in the background air after  $\sim 2$  h of aging, indicating net  $O_3$  formation in this modeled plume. Note that in previous studies,  $O_3$  is not always found to be enhanced relative to the background air especially in more aged (e.g., a few days or older) biomass burning plumes (Alvarado et al., 2010; Parrington et al., 2013). Because of the highly simplified VOC chemistry used in this model, we do not intend to further investigate  $O_3$  formation and variability, which is beyond the scope of this study. But we show that the observed cross-transect variations in  $O_3$  can be qualitatively explained by including simple chemistry with a turbulence-resolving model.

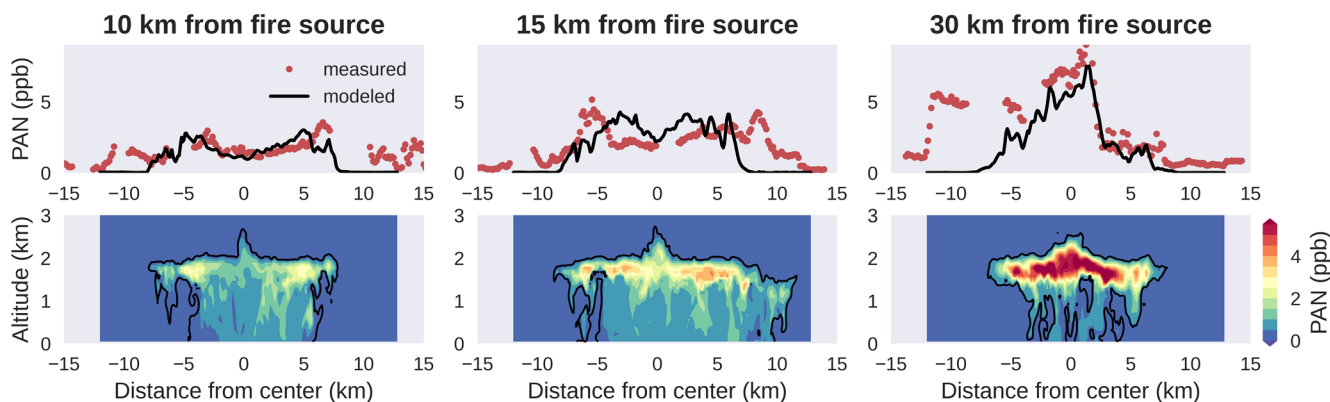


**Figure 8.** Measured peroxyacetyl nitrate (PAN; top) during Segment B and modeled PAN cross sections (bottom) at 10, 15, and 30 km downwind of the fire source. Also shown in the top panel are the modeled PAN sampled at the same distance away from the fire, at  $\sim 2$  km above the model surface.

### 6.2. Elevated PAN Levels at the Plume Edges

PAN is an important reservoir of  $\text{NO}_x$ . Previous studies have reported rapid PAN formation in biomass burning plumes (Alvarado et al., 2010, 2015; Fischer et al., 2018; Jaffe et al., 2013; Liu et al., 2017; Singh et al., 2012). Because of the limited capability in resolving the transport and chemistry of reactive nitrogen species in early biomass burning plumes, large-scale models sometimes partition a fraction of  $\text{NO}_x$  emissions as PAN (Fischer et al., 2014), and this process is subject to uncertainties because of nonlinear of PAN formation (somewhat similar to  $\text{O}_3$ ).

As shown in Figure 3, the modeled plume-wide mean PAN is in reasonable agreement with observations. Figure 8 shows the cross-transect comparison for PAN. Interestingly, at 10 and 15 km downwind, measured PAN is elevated at the edges of the plume compared to that at the center. In particular, at 15 km, the measured PAN is nearly doubled at the edges. The model reproduces this feature at 15 km but tends to overestimate PAN by 2–3 ppb. The edge enhancement of PAN occurs because in the early stage of the plume, PAN formation is limited by the initial OH attack on its VOC precursors, and OH production is more active at the edges of the plume. At 30 km downwind, however, the measured PAN is spread out in a wider range than the model predicts, similar to a few other compounds (Figures 6 and S5–S8). Overall, PAN formation accounts for 10%–70% of the  $\text{NO}_x$  loss in this modeled plume. In summary, the observed PAN shows interesting core–edge differences in the early stage of the plume, corroborating faster photochemical aging at the edges of the plume. This effect may be largely diminished in the later stages of the plume, because dilution further lowers the aerosol loading inside the plume, and hence the suppression of photochemistry inside the plume becomes weaker. Notably, elevated PAN is often found outside the studied plume (i.e., other pollutants such as CO are close to the background levels), providing additional evidence of possible diffused/aged smoke.

### 6.3. Furans as a Fire Tracer and Indicator of Photochemical Aging

In this section, we discuss the simplified furan chemical mechanism included in the LES model (Table S1), as well as one of its unique oxidation products, maleic anhydride. For simplicity, “furan” in this model is a lumped species representing total furan species, and the modeled furan is compared to the TOGA-ToF measurements (sum of furan, 2-methylfuran, 3-methylfuran, and furfural). We do not compare the modeled furans to the PTR-ToF-MS measurements during Segment B since secondary products and lesser-reactive isomers likely result in measurement biases after several hours of oxidation (Coggon et al., 2019; Koss et al., 2018).

Furans are primarily emitted from fire, and their major sink is the reaction with OH radicals, and to a lesser extent, with  $\text{O}_3$  and  $\text{NO}_3$  (Coggon et al., 2019). Figure S9 shows the measured and modeled furans. As shown, the modeled and measured furan show reasonable agreement at 15 and 20 km downwind, but not at 30 km. Its oxidation product, maleic anhydride, however, is enhanced at the edges according to the

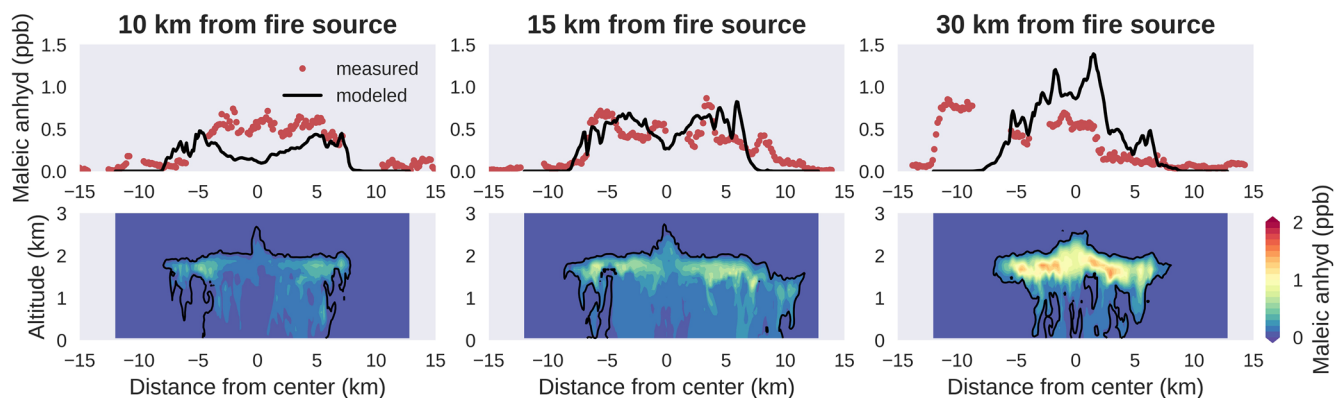


**Figure 9.** PTR-ToF-MS measured maleic anhydride (top) during Segment B and modeled maleic anhydride cross sections (bottom) at 10, 15, and 30 km downwind of the fire source. Also shown in the top panel are the modeled maleic anhydride sampled at the same distance from the fire, at  $\sim 2$  km above the model surface.

measurements at 15 km downwind. Such core-edge discrepancy is consistent with PAN (Section 6.2) and also implies faster photochemical aging at the plume edges. This core-edge discrepancy at 15 km is qualitatively captured by the model (Figure 9). At 10 km, the model also predicts similar core-edge discrepancy. The measured maleic anhydride at 10 km, however, shows a peak at the center of the transect in addition to the two peaks at the edges. This might imply that perhaps a small fraction of maleic anhydride may be directly emitted from the fire source. Maleic anhydride emissions have not been reported in the literature, but a reanalysis of measurements conducted during the FIREX Firelab 2016 study (Coggon et al., 2019; Koss et al., 2018) shows that PTR-ToF-MS measurements of maleic anhydride represent 1%–2% of furan emissions, suggesting that emissions likely contribute to higher plume center mixing ratios at 10 km downwind.

The impact of plume chemical heterogeneity on furan decay is also examined using the modeling results. We discussed in Sections 5 and 6.1 that ozonolysis and  $\text{NO}_3$  oxidation may be active in optically dense smoke, and furan can be oxidized by  $\text{O}_3$ , and  $\text{NO}_3$  as well. We found that OH oxidation is the dominant furan loss pathway, accounting for 78%–89% of total furan loss. Ozonolysis and  $\text{NO}_3$  oxidation account for up to 16% and 7% of total furan loss, respectively. The relative importance of the three oxidation pathways evolves with time: OH oxidation accounts for 3E;90% in the early stage, while ozonolysis and  $\text{NO}_3$  oxidation together contribute to 3C;10% furan oxidation in the early stage. Further downwind, with the gradual recovery of  $\text{O}_3$ , the contribution of ozonolysis increases to up to  $\sim 30\%$  at 30 km downwind, where  $\text{NO}_3$  oxidation also contributes to another  $\sim 20\%$  of total furan loss.  $\text{NO}_3$  oxidation mostly occur in the lower part of the plume, while furan mostly exists in the bulk of the plume aloft. Therefore, the  $\text{NO}_3$  oxidation is partially affected by the plume dynamics. The impact of chemical heterogeneity on the overall VOC reactivity is challenging to represent in small-scale Lagrangian-type models or large-scale models with coarser spatial resolutions.

#### 6.4. HONO: Secondary Production, Impact of Plume Dynamics

HONO is an important precursor of OH radicals in the atmosphere and is emitted from wildland fires (Peng et al., 2020; Theys et al., 2020). In this modeling work, we include both primary HONO emission and secondary HONO formation from  $\text{NO}_2$  heterogeneous reaction on BC and OC aerosols (both reasonably well captured by the model, Figures S7 and S8). The reactive uptake coefficient of  $\text{NO}_2$  is mostly on the order of  $10^{-5}$  to  $10^{-4}$  in the literature (Ammann et al., 2013). Therefore, we assume the  $\text{NO}_2$  uptake coefficient on aerosols is  $5 \times 10^{-5}$  in this work. Model sensitivity tests are also performed to examine the possible secondary HONO production. As for the primary HONO emission, it depends on the fuel type, which is primarily grassland with tall grass, timber, and brush in this region (<https://inciweb.nwccg.gov/>), and the average HONO/ $\text{NO}$  emission ratio (molar basis) for savannah/grassland and temperate forest is 12% and 7%, respectively (Andreae, 2019). This is consistent with a recent laboratory study in which HONO accounts for 13% of  $\text{NO}$  produced from stack fires (Roberts et al., 2020). In this work, we found a fire HONO emission of 11% of fire  $\text{NO}$  emission (molar basis) yields the best agreement when compared to airborne HONO measurements



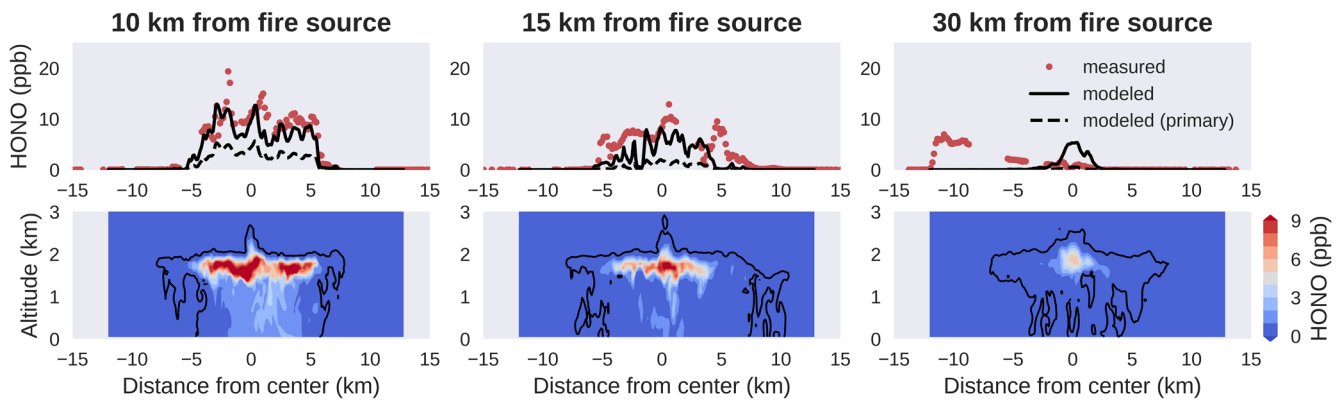
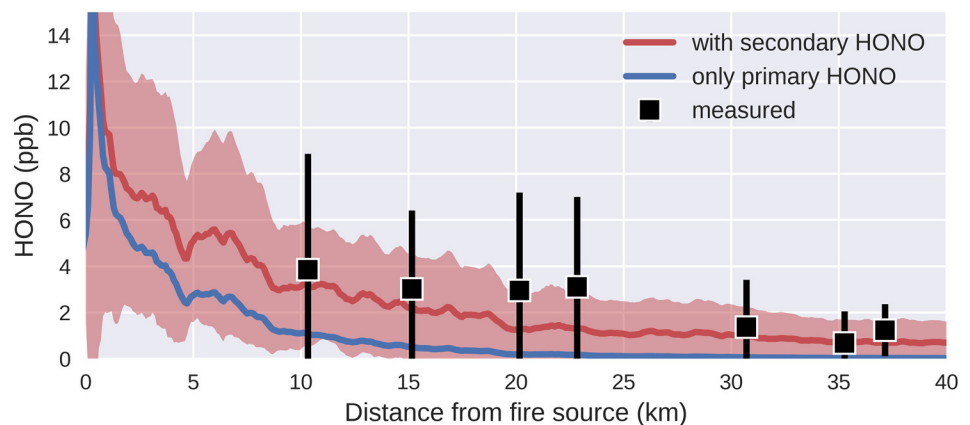


**Figure 10.** Measured HONO (top) during Segment B and modeled HONO cross sections (bottom) at 10, 15, and 30 km downwind of the fire source. Also shown in the top panel are the modeled HONO sampled at the same distance away from the fire (solid black line: with secondary HONO production from  $\text{NO}_2$  heterogeneous reaction; dashed black line: with only primary HONO).

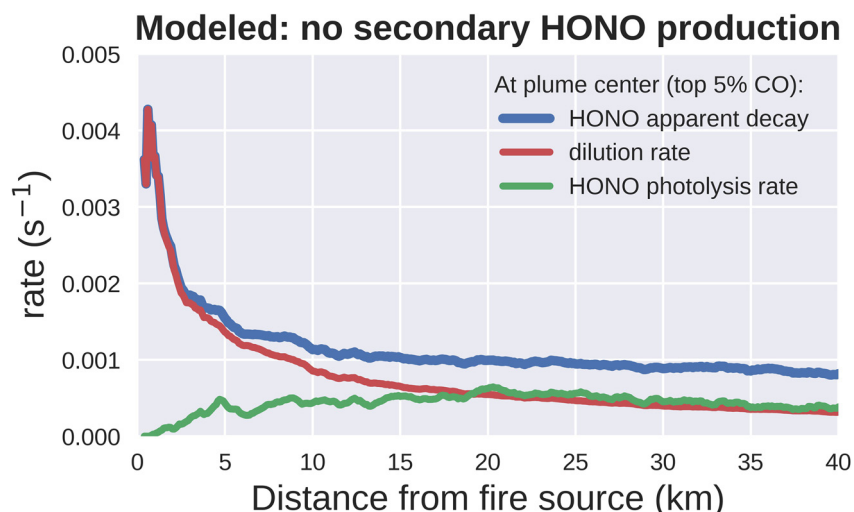
(Figure 3): modeled plume-wide mean HONO exceeded 10 ppb in the very beginning stage of the plume, which then decreased to 2–4 ppb at 10–25 km downwind and eventually to 1–2 ppb at 30–40 km downwind.

Figure 10 shows the cross-transect comparison for HONO. As shown, the measurements suggest that HONO is concentrated at the center of the plume, and the modeled HONO levels across the transects show good agreement with observations, especially in the early stage (10 and 15 km downwind). The model also shows that HONO is always depleted at the edges, especially the upper edge of the plume (Figure 10). The cross-transect comparison for HONO/ $\text{NO}_2$  ratio is given in Figure S10. This ratio remains fairly constant at the center of the modeled plume (with secondary HONO production) but rapidly decreases at the edges of the plume. At 30 km downwind, the model drastically overestimates HONO, mainly due to the overestimation in  $\text{NO}_x$  (Figure S5). This is likely because the sink of  $\text{NO}_x$  is not well captured by this highly condensed chemical mechanism, and future development is needed to refine the  $\text{NO}_x$  budget in this mechanism. Notably, we discussed previously that the model fails to predict the plume profile at 30 km and model captures only one of them (Figures 6, 8, 9 and S5–S8). Figures 10 and S5 show that the modeled peaks HONO and  $\text{NO}_x$  are consistent with observations, yet the model places the plume in the wrong location. This may also imply a change in meteorological condition which alters the plume transport that is not captured by the simple model configuration.

We now discuss the potential secondary HONO production from  $\text{NO}_2$  heterogeneous reactions on aerosols in the modeled plume. As shown in Figures 10 and 11, the model simulation with secondary HONO



**Figure 11.** Measured plume-wide averages of HONO compared to modeled in different model scenarios: with both primary and secondary HONO (dark red, same as that in Figure 3), with only primary HONO and no secondary HONO production (blue).



**Figure 12.** Modeled apparent HONO decay rate (first order) at the center of the plume, as well as the modeled dilution rate and local HONO photolysis rate also at the center. This plot is created using the model simulation without secondary HONO production. Plume center is defined with top 5% modeled CO.

production yields best agreement with observations. Without secondary HONO production, in order to capture the detected HONO levels at 10–15 km downwind, primary HONO emission needs to be increased by a factor of  $\sim 5$  (i.e., about half of NO emission), which still underestimates HONO in the later stage ( $\geq 20$  km downwind). The primary HONO emission contributes substantially to the total HONO levels in the early stage: the modeling results suggest that  $\sim 93\%$  HONO in the early stage is from primary emission, which decreases to 55% at 40 km downwind (observed HONO:  $1.2 \pm 1.1$  ppb at 37 km downwind, Figure 3). Note that the modeled simulation with heterogeneous conversion from  $\text{NO}_2$  to HONO may not necessarily mean a considerable increase in HONO/ $\text{NO}_2$  ratio (Figure S10). To sum up, although no direct evidence can be provided in this work, our combined observational and modeling analysis does suggest that a secondary HONO source better explains the observed HONO levels and variability in this particular plume.

We now take HONO as an example to demonstrate the impact of plume dynamics on the chemical evolution. We showed in Figure 4 that the modeled plume dilution (mixing) is faster in the early stage (driven by strong updraft and entrainment) but is maintained relatively constant in the later stage. The physical mixing within the plume may pose a limiting factor for slow chemical reactions. At the center of the plume, solar radiation is suppressed and hence HONO photolysis is low, leading to a local photolysis lifetime of half an hour or longer. However, as shown in Figure 12, the apparent decay rate of HONO at the center of the plume is nearly 9 times faster than the local photolysis rate but is very close to the physical dilution. That is, although in the early stage photochemistry is slow in the majority of the plume, HONO still decays fairly fast—with an effective lifetime of several minutes at the dark center of the plume. The rapid mixing brings HONO from the center of the plume to the edges and upper part, where HONO is quickly destroyed via photolysis. Even at 40 km downwind, physical mixing still contributes to half of the apparent HONO decay at the center of the modeled plume. This exercise demonstrates the importance of plume dynamics in the chemical evolution in fresh biomass burning plumes.

HONO photolysis is the most important primary OH source in this modeled plume, while other primary OH sources (such as the photolysis of  $\text{O}_3$  and aldehydes) are 1–2 orders of magnitude weaker (Figure S11). In addition to the primary OH sources, secondary OH sources (i.e., recycled from  $\text{HO}_2$ ) also play a key role in the simulated plume, which is on average an order of magnitude higher than the primary OH source (Figure S11), implying an efficient  $\text{HO}_x$  recycling in this modeled plume mediated by  $\text{NO}_x$ . This secondary  $\text{HO}_x$  source also efficiently propagates  $\text{HO}_x$  chemistry into the darker interior of the plume, while photons (that can trigger photochemical reactions) are quickly quenched at the edges and do not reach the bulk of optically dense plumes (e.g., Figure 5). In summary, this section highlights the importance of HONO in

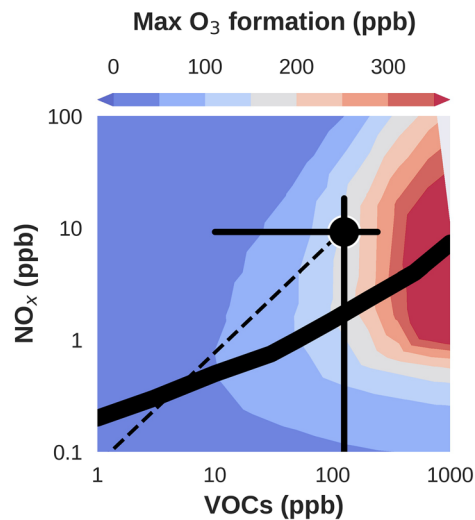


**Figure 13.** Sensitivities of maximum  $O_3$  formation as a function of fire-emitted  $NO_x$  and nonmethane volatile organic compounds (VOCs). The thick black line represents the transition between the  $NO_x$ -saturated and the  $NO_x$ -limited regimes. The circle/error bars represent the airborne measurements averaged during the Segment B of Williams Flats Fire (August 3–4, 2019). The thin dashed line is the 1:1 dilution line for Williams Flats Fire.

wildland fire plumes. The reactive uptake coefficient of  $NO_2$  as well as the dependency on particle type and other parameters or conditions warrants further investigation.

## 7. Implications for Models With Coarser Horizontal Resolutions

In principle, LES schemes resolve major (large) eddies, through which momentum, energy, and other passive scalars are transported. This sets the upper limit of the horizontal grid size in LES models to about 0.1 km. Most planetary boundary layer (PBL) schemes (widely used in regional and global chemical transport models) are not designed to resolve the energy-bearing eddies, which are parameterized as subgrid processes instead. This sets the lower limit of the horizontal grid size of most PBL schemes to about 1 km. Moreover, operating with small grid sizes (or high horizontal resolution) often also requires shorter integration time steps, which also leads to an increase in computational cost. Currently, most regional chemical transport models are operated at horizontal grid resolutions of a few to tens of km. In this section, we discuss the impact of grid resolution on the chemical evolution of wildland fire plumes.

Biomass burning emission inventories report the emissions of pollutants on a mass basis. When using an emission inventory in a particular model, the emissions need to be regridded into the horizontal resolution at which the model is operated. Usually, an area-weighted interpolation

method would be used since the total amount of emitted pollutants needs to be conserved. If the model horizontal grid size is larger than the fire size, to maintain mass conservation, all fire-emitted tracers are immediately diluted within the grid cell, leading to an instantaneous numerical dilution. For instance, the area of the fire source in this model is  $0.6 \text{ km}^2$ , and if mimicking this particular fire using a model with 4-km grid resolution (with same vertical resolution, assuming the fire source is not spread into multiple grids), the emission fluxes are reduced by a factor of  $26.7 (4^2/0.6)$ ; if the model grid resolution is 1 km, the emission fluxes are still reduced by a factor of  $1.5 (1^2/0.6)$ . The atmospheric chemical system is highly nonlinear, especially the  $O_3$  chemistry, such that dilution may lead to a shift in chemical regimes. Figure 13 shows the sensitivity of maximum  $O_3$  formation as a function of fire-emitted  $NO_x$  and VOCs. This plot is created using a box model (same as that used in Wang et al., 2019) with a near-explicit chemical mechanism (MCM v3.3.1), including furan chemistry (Coggon et al., 2019), and constrained to airborne measurements collected from Segment B (in-plume only) from the Williams Flats Fire. Also shown on this plot is the dashed line representing the impact of dilution—numerical or otherwise. The dilution always leads to a reduction in the maximum  $O_3$  formation potential, but the magnitude of such reduction depends on the chemical regime. As shown, the dilution line for the Williams Flats Fire is close to the “ridge” (transition between  $NO_x$ /VOC-sensitive regimes), and hence dilution would lead to a rapid decrease in  $O_3$  formation potential, and perhaps a change in the chemical regime as well (from  $NO_x$ -saturated/VOC-sensitive regime to the VOC-saturate/ $NO_x$ -sensitive regime).

Figure 14 illustrates the impact of model grid resolution on fire-induced column  $O_3$  and  $NO_2$ , by comparing the results from the 0.1-km LES model to that from two model configurations with coarser horizontal resolutions: 1 and 4 km. The 1- and 4-km models shown in Figure 14 are configured in the same way as the 0.1-km LES model, except the fire emissions are regridded to 1 and 4 km grids accordingly (mass conserved), and the Yonsei University (YSU) PBL scheme (Hong et al., 2006) are used in the 1 and 4 km models. As discussed before, the underlying principle of LES sets the upper limit to the grid spacing to about 0.1 km, therefore a grid spacing of 1 or 4 km is inappropriate for LES.

As shown, the 0.1 km model reveals  $O_3$  suppression in the first  $\sim 14$  km or so, and  $O_3$  enhancement is visible starting from  $\sim 14$  km. At  $X = 40\text{--}50$  km, the predicted  $O_3$  column reaches  $\sim 3.71 \times 10^{17}$  molecule  $\text{cm}^{-2}$  in the 0.1 km model or  $\sim 0.70 \times 10^{17}$  molecule  $\text{cm}^{-2}$  higher than the background  $O_3$  column ( $\sim 3.01 \times 10^{17}$

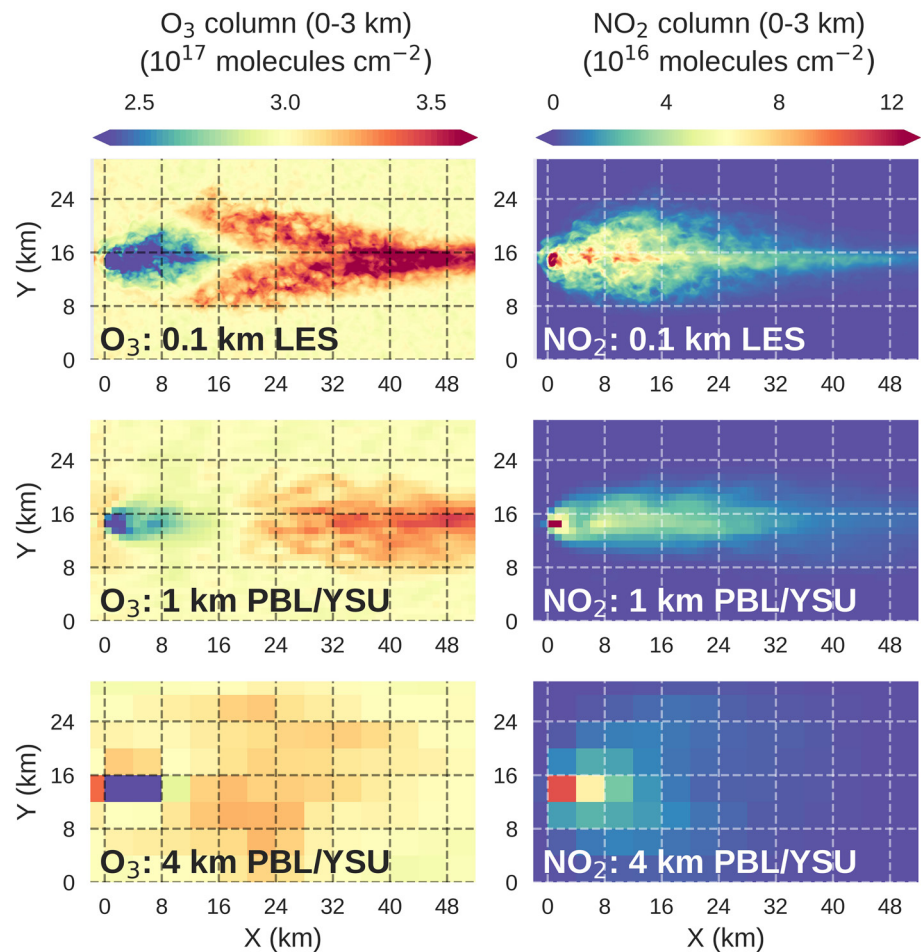


**Figure 14.** Modeled lower tropospheric column densities of  $\text{O}_3$  and  $\text{NO}_2$  with horizontal resolution of 0.1, 1, and 4 km. All column densities are integrated from the surface to 3 km. The 0.1 km resolution model is the large eddy simulation (LES) model that is discussed throughout this work, while the 1 km and the 4 km models are using Yonsei University (YSU) scheme and are driven by the same fire emissions but regridded accordingly. Other configurations in the 1 and 4 km models are identical to the 0.1 km model. See main text for more details.

molecule  $\text{cm}^{-2}$ ). Both the 1 and 4 km models capture the  $\text{O}_3$  suppression in the first  $\sim 10$  km or so. However, the maximum  $\text{O}_3$  enhancement in the 4 km model appears at  $X = 16\text{--}28$  km at  $\sim 3.27 \times 10^{17}$  molecule  $\text{cm}^{-2}$  or  $0.27 \times 10^{17}$  molecule  $\text{cm}^{-2}$  higher than the background, and the  $\text{O}_3$  enhancement quickly diminished beyond  $X = \sim 32$  km. That is, the 4 km model does not efficiently transport the fire-emitted  $\text{O}_3$  precursors, and the column  $\text{O}_3$  enhancement is underestimated by 61%. The 1 km model better captures the maximum  $\text{O}_3$  enhancement ( $\sim 3.47 \times 10^{17}$  molecule  $\text{cm}^{-2}$  or  $\sim 0.46 \times 10^{17}$  molecule  $\text{cm}^{-2}$  above the background level, 34% lower than the 0.1 km LES model).  $\text{NO}_2$  column shows similar trends as well: the 4 km model shows a fire-induced  $\text{NO}_2$  column enhancement only in the first  $\sim 20$  km or so, while the 0.1 km model efficiently transports the fire-induced  $\text{NO}_2$  column to  $\sim 40$  km. The 1 km model also better captures the spatial variation of the  $\text{NO}_2$  column in the downwind direction. Interestingly, all three models are driven by the same external forcing, yet the plume in the 4 km model is much wider than that in the 0.1 km LES model, possibly due to numerical diffusion (a known issue in finite volume Eulerian grids). The 1 km model appears to predict a narrower plume width than the 0.1 km LES model. This is mainly because of the alignment of the fire source. In the 0.1 km LES model, in order to match the observed plume width (Figures 6 and S4–S8), the fire source is tuned into a rectangular shape of 0.3 km (X)  $\times$  2.2 km (Y), while in the 1 km model the fire source is just one 1  $\times$  1 km grid. The high horizontal resolution of the 0.1 km LES model allows a better representation of the shape and the orientation of the fire source as well. Overall, this exercise shows results that are consistent with those in Figure 13, that the numerical dilution leads to a decrease in  $\text{O}_3$  formation potential,



with a reduced efficiency of transporting smoke to the downwind direction. The 1 km model performs better than the 4 km model in terms of efficiently transporting the smoke and predicting the O<sub>3</sub> formation.

## 8. What Horizontal Resolution Should Air Quality Models Target?

The effects of spatial resolution on the chemical evolution in biomass burning plumes or similar point-/area-sources have been discussed (Alvarado et al., 2009; van Wees & van der Werf, 2019). In particular, Valin et al. (2011) pointed out that in order to capture the NO<sub>2</sub> removal in the urban plumes, the model resolution has to be in the range of 4–12 km. Most active wildland fire areas are smaller than the urban scale. According to the Fire INventory from NCAR (FINN) version 2 (Wiedinmyer et al., 2011), a widely used biomass burning inventory, 90% of wildfires in 2019 were smaller than 1 km<sup>2</sup> (fire size). Therefore, the impacts of small fires on O<sub>3</sub> formation may be largely reduced in models with coarser spatial resolutions, which is caused by numerical dilution, a bias purely caused by grid resolution.

To represent the smoke transport and O<sub>3</sub> formation associated with wildland fires, in principle, the model grid resolution should be comparable to the active fire source. Although plausible, it remains computationally challenging to perform simulations with LES schemes at regional scale. Considering the computational cost associated with model resolution, we propose that air quality forecast models should target ~1 km horizontal resolution in the near future. We show in this work that a 1 km model can reasonably well capture the transport of NO<sub>x</sub> and O<sub>3</sub> formation associated with a fire area that is ~60% of the grid size. Based again on FINN version 2, in 2019, approximately 17% of wildfires in the U.S. are larger than 0.6 km<sup>2</sup>, and these top 17% wildfires contribute 62% total fire-NO<sub>x</sub> emission, 60% total fire-CO emission, and 61% total nonmethane VOC emissions from fires nationwide. Therefore, an air quality forecast model with ~1 km horizontal resolution can greatly improve our ability to predict wildfire impacts on air quality, which could potentially affect nearly half of the U.S. population (Figure S12).

## 9. Conclusions and Remarks

In this work, a high-resolution turbulence-resolving model, WRF-LES, is coupled to chemistry to study the chemical evolution in a wildland fire plume. The results are evaluated using airborne measurements collected from the Williams Flats Fire during the FIREX-AQ field campaign. The model reveals remarkable chemical heterogeneity that is supported by observations. Major findings are summarized as follows:

1. The strong heat released from the fire source drives rapid plume rise in the very early stage, which also leads to rapid dilution with background air. Dilution and physical mixing greatly affect chemistry inside the plume.
2. O<sub>3</sub> shows considerable heterogeneity inside the plume: Suppressed at the center (due to NO reaction) but may be enhanced at the edges. To our knowledge, our model is the first to capture the observed cross-transect O<sub>3</sub> variations in optically thick biomass burning plumes.
3. PAN and maleic anhydride (from the oxidation of furan, a distinct class of compounds emitted from fires) are also enhanced at the edges of the plume in the early stage, implying faster OH oxidation at the edges.
4. Primary OH production is dominated by HONO photolysis, and HO<sub>x</sub> cycling extends OH radicals deeper into the plume. Although OH oxidation is the major sink of VOCs in daytime plumes, we show that dark chemistry driven by O<sub>3</sub> and NO<sub>3</sub> oxidation may proceed at the same time but mostly in the lower part of (or below) thick plumes.
5. Although this modeling work cannot provide direct evidence of secondary HONO production in the studied plume, we find that observed HONO variability can be best explained by including a secondary HONO production from NO<sub>2</sub> heterogeneous reaction on aerosols.

We acknowledge that the model configuration is highly idealized, and much of the observations remain unexplained by the model. Nevertheless, there are several key take-away messages worth mentioning. First, Lagrangian-type models that explore the chemical evolution in dense fire plumes must specify the plume region being modeled, since it is the edges that largely drive the photochemistry in thick fire plumes. Second, dilution and mixing within the plume are important, which are not constant and may greatly affect

how fast chemistry proceeds inside the plume. Third, we found that HONO and the photons that can trigger HONO photolysis are always segregated in the modeled plume, that is, HONO is always depleted in the edges and the upper part, while  $j(\text{HONO})$  is exclusively elevated in the edges and upper most part of the optically dense smoke (Figure 5). This has implications for satellite HONO retrievals. Recently Theyss et al. (2020) reported the detection of HONO in biomass burning plumes from Tropospheric Monitoring Instrument (TROPOMI), showcasing the remarkable capability of retrieving reactive trace gases such as HONO from this space-borne instrument. High-resolution models with chemistry such as the LES-chemistry model used in this work can better resolve the plume structure and the distributions of trace gases and aerosols, therefore may be used to test remote sensing retrievals for optically dense plumes.

Finally, we showed that model spatial resolution may shift the chemical regime and lead to reduced  $\text{O}_3$  formation potential. For the Williams Flats Fire studied in this work, a model with  $\sim 1$  km horizontal resolution may decently capture the fire-induced  $\text{O}_3$  and  $\text{NO}_2$  enhancement in the downwind direction, but a model with  $\sim 4$  km horizontal resolution may be insufficient to capture the impacts on these short-lived pollutants. We thus propose that regional or national air quality models in the U.S. should target  $\sim 1$  km horizontal resolution in the near future, which may greatly improve our capability to predict the wildfire impacts on air quality for nearly half of the U.S. population.

### Data Availability Statement

The FIREX-AQ campaign data are archived and available from NASA Langley Research Center (<https://www-air.larc.nasa.gov/missions/firex-aq/>). The WRF model is available from GitHub (<https://github.com/wrf-model/WRF>). The gridded U.S. population density data (Figure S12) are from Center for International Earth Science Information Network Columbia University (2020).

### Acknowledgments

S.-Y. Wang was partially supported by the FIREX-AQ project (80NSSC18K0681). S. R. Hall and K. Ullmann were partially supported by the NASA FIREX-AQ project (80NSSC18K0638). The computing and data storage resources, including the Cheyenne supercomputer (<https://doi.org/10.5065/D6RX99HX>), were provided by the Computational and Information Systems Laboratory (CISL) at NCAR. NCAR is a major facility sponsored by the NSF under Cooperative Agreement No. 1852977. The authors thank the FIREX-AQ Science Team for their exceptional professionalism in support of this mission. The authors thank Glenn Wolfe, Thomas Hanisco (NASA Goddard), Joshua P. Schwarz, Joseph M. Katich (NOAA/CSL), Jose-Luis Jimenez, Pedro Campuzano-Jost, Douglas Day, Hongyu Guo, Demetrios Pagonis, Mindy Schueneman (CU Boulder), and Alan Fried (CU Boulder) for their efforts in collecting the measurements. Stuart McKeen, Rebecca Schwantes (CIRES/NOAA CSL), Brian McDonald, and Gregory Frost (NOAA CSL) are acknowledged for helpful discussion. The authors thank J. Dudhia and M. Barth (NCAR) for the support regarding the LES modeling.

### References

- Abatzoglou, J. T., & Williams, A. P. (2016). Impact of anthropogenic climate change on wildfire across western US forests. *Proceedings of the National Academy of Sciences of the United States of America*, 113(42), 11770–11775. <https://doi.org/10.1073/pnas.1607171113>
- Agee, E., & Gluhovsky, A. (1999). LES model sensitivities to domains, grids, and large-eddy timescales. *Journal of the Atmospheric Sciences*, 56(4), 599–604. [https://doi.org/10.1175/1520-0469\(1999\)056%3C;0599:LMSTDG%3E;2.0.CO;2](https://doi.org/10.1175/1520-0469(1999)056%3C;0599:LMSTDG%3E;2.0.CO;2)
- Alvarado, M. J., Logan, J. A., Mao, J., Apel, E., Riemer, D., Blake, D., et al. (2010). Nitrogen oxides and PAN in plumes from boreal fires during ARCTAS-B and their impact on ozone: An integrated analysis of aircraft and satellite observations. *Atmospheric Chemistry and Physics*, 10(20), 9739–9760. <https://doi.org/10.5194/acp-10-9739-2010>
- Alvarado, M. J., Lonsdale, C. R., Yokelson, R. J., Akagi, S. K., Coe, H., Craven, J. S., et al. (2015). Investigating the links between ozone and organic aerosol chemistry in a biomass burning plume from a prescribed fire in California chaparral. *Atmospheric Chemistry and Physics*, 15(12), 6667–6688. <https://doi.org/10.5194/acp-15-6667-2015>
- Alvarado, M. J., & Prinn, R. G. (2009). Formation of ozone and growth of aerosols in young smoke plumes from biomass burning: 1. Lagrangian parcel studies. *Journal of Geophysical Research*, 114, D09306. <https://doi.org/10.1029/2008JD011144>
- Alvarado, M. J., Wang, C., & Prinn, R. G. (2009). Formation of ozone and growth of aerosols in young smoke plumes from biomass burning: 2. Three-dimensional Eulerian studies. *Journal of Geophysical Research*, 114, D09307. <https://doi.org/10.1029/2008JD011186>
- Ammann, M., Cox, R. A., Crowley, J. N., Jenkin, M. E., Mellouki, A., Rossi, M. J., et al. (2013). Evaluated kinetic and photochemical data for atmospheric chemistry: Volume VI—Heterogeneous reactions with liquid substrates. *Atmospheric Chemistry and Physics*, 13(16), 8045–8228. <https://doi.org/10.5194/acp-13-8045-2013>
- Andreae, M. O. (2019). Emission of trace gases and aerosols from biomass burning—An updated assessment. *Atmospheric Chemistry and Physics*, 19(13), 8523–8546. <https://doi.org/10.5194/acp-19-8523-2019>
- Brock, C. A., Washenfelder, R. A., Trainer, M., Ryerson, T. B., Wilson, J. C., Reeves, J. M., et al. (2002). Particle growth in the plumes of coal-fired power plants. *Journal of Geophysical Research*, 107(D12), 4155. <https://doi.org/10.1029/2001JD001062>
- Center for International Earth Science Information Network, Columbia University. (2020). *Gridded Population of the World, version 4 (GPWv4): Population density revision UN WPP country totals, revision 11*. NASA Socioeconomic Data and Applications Center (SEDAC). <https://doi.org/10.7927/H4F47M65>
- Coen, J. (2013). *Modeling wildland fires: A description of the Coupled Atmosphere-Wildland Fire Environment model (CAWFE)*. NCAR Earth System Laboratory. <https://doi.org/10.5065/D6K64G2G>
- Coggon, M. M., Lim, C. Y., Koss, A. R., Sekimoto, K., Yuan, B., Gilman, J. B., et al. (2019). OH chemistry of non-methane organic gases (NMOGs) emitted from laboratory and ambient biomass burning smoke: Evaluating the influence of furans and oxygenated aromatics on ozone and secondary NMOG formation. *Atmospheric Chemistry and Physics*, 19(23), 14875–14899. <https://doi.org/10.5194/acp-19-14875-2019>
- David, L. M., Ravishankara, A. R., Brey, S. J., Fischer, E. V., Volckens, J., & Kreidenweis, S. (2021). Could the exception become the rule? “Uncontrollable” air pollution events in the US due to wildland fires. *Environmental Research Letters*, 16, 034029. <https://doi.org/10.1088/1748-9326/abe1f3>
- de Roode, S. R., Duynkerke, P. G., & Jonker, H. J. J. (2004). Large-eddy simulation: How large is large enough? *Journal of the Atmospheric Sciences*, 61(4), 403–421. [https://doi.org/10.1175/1520-0469\(2004\)061%3C;0403:LSHLL%3E;2.0.CO;2](https://doi.org/10.1175/1520-0469(2004)061%3C;0403:LSHLL%3E;2.0.CO;2)
- Doerr, S. H., & Santin, C. (2016). Global trends in wildfire and its impacts: Perceptions versus realities in a changing world. *Philosophical Transactions of the Royal Society B: Biological Sciences*, 371(1696), 20150345. <https://doi.org/10.1098/rstb.2015.0345>

- Fischer, E. V., Jacob, D. J., Yantosca, R. M., Sulprizio, M. P., Millet, D. B., Mao, J., et al. (2014). Atmospheric peroxyacetyl nitrate (PAN): A global budget and source attribution. *Atmospheric Chemistry and Physics*, 14(5), 2679–2698. <https://doi.org/10.5194/acp-14-2679-2014>
- Fischer, E. V., Zhu, L., Payne, V. H., Worden, J. R., Jiang, Z., Kulawik, S. S., et al. (2018). Using TES retrievals to investigate PAN in North American biomass burning plumes. *Atmospheric Chemistry and Physics*, 18(8), 5639–5653. <https://doi.org/10.5194/acp-18-5639-2018>
- Flannigan, M., Cantin, A. S., de Groot, W. J., Wotton, M., Newbery, A., & Gowman, L. M. (2013). Global wildland fire season severity in the 21st century. *Forest Ecology and Management*, 294, 54–61. <https://doi.org/10.1016/j.foreco.2012.10.022>
- Hodshire, A. L., Akherati, A., Alvarado, M. J., Brown-Steiner, B., Jathar, S. H., Jimenez, J. L., et al. (2019). Aging effects on biomass burning aerosol mass and composition: A critical review of field and laboratory studies. *Environmental Science & Technology*, 53(17), 10007–10022. <https://doi.org/10.1021/acs.est.9b02588>
- Hodshire, A. L., Bian, Q., Ramnarine, E., Lonsdale, C. R., Alvarado, M. J., Kreidenweis, S. M., et al. (2019). More than emissions and chemistry: Fire size, dilution, and background aerosol also greatly influence near-field biomass burning aerosol aging. *Journal of Geophysical Research: Atmospheres*, 124, 5589–5611. <https://doi.org/10.1029/2018JD029674>
- Hong, S.-Y., Noh, Y., & Dudhia, J. (2006). A new vertical diffusion package with an explicit treatment of entrainment processes. *Monthly Weather Review*, 134(9), 2318–2341. <https://doi.org/10.1175/MWR3199.1>
- Jaffe, D. A., O'Neill, S. M., Larkin, N. K., Holder, A. L., Peterson, D. L., Halofsky, J. E., & Rappold, A. G. (2020). Wildfire and prescribed burning impacts on air quality in the United States. *Journal of the Air & Waste Management Association*, 70(6), 583–615. <https://doi.org/10.1080/10962247.2020.1749731>
- Jaffe, D. A., Wigder, N., Downey, N., Pfister, G., Boynard, A., & Reid, S. B. (2013). Impact of wildfires on ozone exceptional events in the western U.S. *Environmental Science & Technology*, 47(19), 11065–11072. <https://doi.org/10.1021/es402164f>
- Knote, C., Hodzic, A., Jimenez, J. L., Volkamer, R., Orlando, J. J., Baidar, S., et al. (2014). Simulation of semi-explicit mechanisms of SOA formation from glyoxal in aerosol in a 3-D model. *Atmospheric Chemistry and Physics*, 14(12), 6213–6239. <https://doi.org/10.5194/acp-14-6213-2014>
- Kodros, J. K., Papanastasiou, D. K., Paglione, M., Masiol, M., Squizzato, S., Florou, K., et al. (2020). Rapid dark aging of biomass burning as an overlooked source of oxidized organic aerosol. *Proceedings of the National Academy of Sciences of the United States of America*, 117, 33028–33033. <https://doi.org/10.1073/pnas.2010365117>
- Konovalov, I. B., Beekmann, M., Golovushkin, N. A., & Andreae, M. O. (2019). Nonlinear behavior of organic aerosol in biomass burning plumes: A microphysical model analysis. *Atmospheric Chemistry and Physics*, 19(19), 12091–12119. <https://doi.org/10.5194/acp-19-12091-2019>
- Koss, A. R., Sekimoto, K., Gilman, J. B., Selimovic, V., Coggon, M. M., Zarzana, K. J., et al. (2018). Non-methane organic gas emissions from biomass burning: Identification, quantification, and emission factors from PTR-ToF during the FIREX 2016 laboratory experiment. *Atmospheric Chemistry and Physics*, 18(5), 3299–3319. <https://doi.org/10.5194/acp-18-3299-2018>
- Li, F., Zhang, X., Kondragunta, S., Schmidt, C. C., & Holmes, C. D. (2020). A preliminary evaluation of GOES-16 active fire product using Landsat-8 and VIIRS active fire data, and ground-based prescribed fire records. *Remote Sensing of Environment*, 237, 111600. <https://doi.org/10.1016/j.rse.2019.111600>
- Liu, X., Huey, L. G., Yokelson, R. J., Selimovic, V., Simpson, I. J., Müller, M., et al. (2017). Airborne measurements of western U.S. wildfire emissions: Comparison with prescribed burning and air quality implications. *Journal of Geophysical Research: Atmospheres*, 122, 6108–6129. <https://doi.org/10.1002/2016JD026315>
- Lu, X., Zhang, L., Yue, X., Zhang, J., Jaffe, D. A., Stohl, A., et al. (2016). Wildfire influences on the variability and trend of summer surface ozone in the mountainous western United States. *Atmospheric Chemistry and Physics*, 16(22), 14687–14702. <https://doi.org/10.5194/acp-16-14687-2016>
- Mandel, J., Beezley, J. D., & Kochanski, A. K. (2011). Coupled atmosphere-wildland fire modeling with WRF 3.3 and SFIRE 2011. *Geoscientific Model Development*, 4(3), 591–610. <https://doi.org/10.5194/gmd-4-591-2011>
- Martinuzzi, S., Stewart, S. I., Helmers, D. P., Mockrin, M. H., Hammer, R. B., & Radeloff, V. C. (2015). *The 2010 wildland-urban interface of the conterminous United States (Research Map NRS-8, p.124) [Includes Pull-out Map]*. U.S. Department of Agriculture, Forest Service, Northern Research Station. <https://doi.org/10.2737/NRS-RMAP-8>
- Mason, S. A., Trentmann, J., Winterrath, T., Yokelson, R. J., Christian, T. J., Carlson, L. J., et al. (2006). Intercomparison of two box models of the chemical evolution in biomass-burning smoke plumes. *Journal of Atmospheric Chemistry*, 55(3), 273–297. <https://doi.org/10.1007/s10874-006-9039-5>
- McClure, C. D., & Jaffe, D. A. (2018). US particulate matter air quality improves except in wildfire-prone areas. *Proceedings of the National Academy of Sciences of the United States of America*, 115(31), 7901–7906. <https://doi.org/10.1073/pnas.1804353115>
- Moeng, C.-H., Dudhia, J., Klemp, J., & Sullivan, P. (2007). Examining two-way grid nesting for large eddy simulation of the PBL using the WRF model. *Monthly Weather Review*, 135(6), 2295–2311. <https://doi.org/10.1175/MWR3406.1>
- Palm, B. B., Peng, Q., Fredrickson, C. D., Lee, B. H., Garofalo, L. A., Pothier, M. A., et al. (2020). Quantification of organic aerosol and brown carbon evolution in fresh wildfire plumes. *Proceedings of the National Academy of Sciences of the United States of America*, 117(47), 29469–29477. <https://doi.org/10.1073/pnas.2012218117>
- Parrington, M., Palmer, P. I., Lewis, A. C., Lee, J. D., Rickard, A. R., Di Carlo, P., et al. (2013). Ozone photochemistry in boreal biomass burning plumes. *Atmospheric Chemistry and Physics*, 13(15), 7321–7341. <https://doi.org/10.5194/acp-13-7321-2013>
- Peng, Q., Palm, B. B., Melander, K. E., Lee, B. H., Hall, S. R., Ullmann, K., et al. (2020). HONO emissions from western U.S. wildfires provide dominant radical source in fresh wildfire smoke. *Environmental Science & Technology*, 54(10), 5954–5963. <https://doi.org/10.1021/acs.est.0c00126>
- Reid, C. E., Brauer, M., Johnston, F. H., Jerrett, M., Balmes, J. R., & Elliott, C. T. (2016). Critical review of health impacts of wildfire smoke exposure. *Environmental Health Perspectives*, 124(9), 1334–1343. <https://doi.org/10.1289/ehp.1409277>
- Roberts, J. M., Stockwell, C. E., Yokelson, R. J., de Gouw, J., Liu, Y., Selimovic, V., et al. (2020). The nitrogen budget of laboratory-simulated western US wildfires during the FIREX 2016 Fire Lab study. *Atmospheric Chemistry and Physics*, 20(14), 8807–8826. <https://doi.org/10.5194/acp-20-8807-2020>
- Schwarz, J. P., Gao, R. S., Spackman, J. R., Watts, L. A., Thomson, D. S., Fahey, D. W., et al. (2008). Measurement of the mixing state, mass, and optical size of individual black carbon particles in urban and biomass burning emissions. *Geophysical Research Letters*, 35, L13810. <https://doi.org/10.1029/2008GL033968>
- Singh, H. B., Cai, C., Kaduwela, A., Weinheimer, A., Wisthaler, A. (2012). Interactions of fire emissions and urban pollution over California: Ozone formation and air quality simulations. *Atmospheric Environment*, 56, 45–51. <https://doi.org/10.1016/j.atmosenv.2012.03.046>
- Theys, N., Volkamer, R., Müller, J.-F., Zarzana, K. J., Kille, N., Clarisse, L., et al. (2020). Global nitrous acid emissions and levels of regional oxidants enhanced by wildfires. *Nature Geoscience*, 13(10), 681–686. <https://doi.org/10.1038/s41561-020-0637-7>

- Tie, X., Madronich, S., Walters, S., Zhang, R., Rasch, P., & Collins, W. (2003). Effect of clouds on photolysis and oxidants in the troposphere. *Journal of Geophysical Research*, *108*(D20), 4642. <https://doi.org/10.1029/2003JD003659>
- Trentmann, J., Andreae, M. O., & Graf, H.-F. (2003). Chemical processes in a young biomass-burning plume. *Journal of Geophysical Research*, *108*(D22), 4705. <https://doi.org/10.1029/2003JD003732>
- Trentmann, J., Andreae, M. O., Graf, H.-F., Hobbs, P. V., Ottmar, R. D., & Trautmann, T. (2002). Simulation of a biomass-burning plume: Comparison of model results with observations. *Journal of Geophysical Research*, *107*(D2), 4013. <https://doi.org/10.1029/2001JD000410>
- Trentmann, J., Früh, B., Boucher, O., Trautmann, T., & Andreae, M. O. (2003). Three-dimensional solar radiation effects on the actinic flux field in a biomass-burning plume. *Journal of Geophysical Research*, *108*(D17), 4558. <https://doi.org/10.1029/2003JD003422>
- Trentmann, J., Yokelson, R. J., Hobbs, P. V., Winterrath, T., Christian, T. J., Andreae, M. O., & Mason, S. A. (2005). An analysis of the chemical processes in the smoke plume from a savanna fire. *Journal of Geophysical Research*, *110*, D12301. <https://doi.org/10.1029/2004JD005628>
- Valin, L. C., Russell, A. R., Hudman, R. C., & Cohen, R. C. (2011). Effects of model resolution on the interpretation of satellite NO<sub>2</sub> observations. *Atmospheric Chemistry and Physics*, *11*(22), 11647–11655. <https://doi.org/10.5194/acp-11-11647-2011>
- von Wees, D., & vander Werf, G. R. (2019). Modelling biomass burning emissions and the effect of spatial resolution: A case study for Africa based on the Global Fire Emissions Database (GFED). *Geoscientific Model Development*, *12*(11), 4681–4703. <https://doi.org/10.5194/gmd-12-4681-2019>
- Wang, S., McNamara, S. M., Moore, C. W., Obrist, D., Steffen, A., Shepson, P. B., et al. (2019). Direct detection of atmospheric atomic bromine leading to mercury and ozone depletion. *Proceedings of the National Academy of Sciences of the United States of America*, *116*, 14479–14484. <https://doi.org/10.1073/pnas.1900613116>
- Westerling, A. L., Hidalgo, H. G., Cayan, D. R., & Swetnam, T. W. (2006). Warming and earlier spring increase western U.S. forest wildfire activity. *Science*, *313*(5789), 940–943. <https://doi.org/10.1126/science.1128834>
- Wiedinmyer, C., Akagi, S. K., Yokelson, R. J., Emmons, L. K., Al-Saadi, J. A., Orlando, J. J., & Soja, A. J. (2011). The fire inventory from NCAR (FINN): A high resolution global model to estimate the emissions from open burning. *Geoscientific Model Development*, *4*(3), 625–641. <https://doi.org/10.5194/gmd-4-625-2011>
- Yokelson, R. J., Christian, T. J., Karl, T. G., & Guenther, A. (2008). The tropical forest and fire emissions experiment: Laboratory fire measurements and synthesis of campaign data. *Atmospheric Chemistry and Physics*, *8*(13), 3509–3527. <https://doi.org/10.5194/acp-8-3509-2008>

## References From the Supporting Information

- Apel, E., Hornbrook, R., Hills, A., Blake, N., Barth, M., Weinheimer, A., et al. (2015). Upper tropospheric ozone production from lightning NO<sub>x</sub>-impacted convection: Smoke ingestion case study from the DC3 campaign. *Journal of Geophysical Research: Atmospheres*, *120*, 2505–2523. <https://doi.org/10.1002/2014JD022121>
- Aschmann, S. M., Nishino, N., Arey, J., & Atkinson, R. (2011). Kinetics of the reactions of OH radicals with 2- and 3-methylfuran, 2, 3- and 2, 5-dimethylfuran, and E- and Z-3-hexene-2, 5-dione, and products of OH + 2, 5-dimethylfuran. *Environmental Science & Technology*, *45*(5), 1859–1865. <https://doi.org/10.1021/es103207k>
- Aschmann, S. M., Nishino, N., Arey, J., & Atkinson, R. (2014). Products of the OH radical-initiated reactions of furan, 2- and 3-methylfuran, and 2, 3- and 2, 5-dimethylfuran in the presence of NO. *The Journal of Physical Chemistry A*, *118*(2), 457–466. <https://doi.org/10.1021/jp410345k>
- Bierbach, A., Barnes, I., & Becker, K. H. (1995). Product and kinetic study of the OH-initiated gas-phase oxidation of furan, 2-methylfuran and furan aldehydes at ≈300 K. *Atmospheric Environment*, *29*(19), 2651–2660. [https://doi.org/10.1016/1352-2310\(95\)00096-H](https://doi.org/10.1016/1352-2310(95)00096-H)
- Cazorla, M., Wolfe, G. M., Bailey, S. A., Swanson, A. K., Arkinson, H. L., & Hanisco, T. F. (2015). A new airborne laser-induced fluorescence instrument for in situ detection of formaldehyde throughout the troposphere and lower stratosphere. *Atmospheric Measurement Techniques*, *8*(2), 541–552. <https://doi.org/10.5194/amt-8-541-2015>
- DeCarlo, P. F., Kimmel, J. R., Trimborn, A., Northway, M. J., Jayne, J. T., Aiken, A. C., et al. (2006). Field-deployable, high-resolution, time-of-flight aerosol mass spectrometer. *Analytical Chemistry*, *78*(24), 8281–8289.
- Hair, J. W., Hostetler, C. A., Cook, A. L., Harper, D. B., Ferrare, R. A., Mack, T. L., et al. (2008). Airborne High Spectral Resolution Lidar for profiling aerosol optical properties. *Applied Optics*, *47*(36), 6734–6752. <https://doi.org/10.1364/AO.47.006734>
- Huey, L. G. (2007). Measurement of trace atmospheric species by chemical ionization mass spectrometry: Speciation of reactive nitrogen and future directions. *Mass Spectrometry Reviews*, *26*(2), 166–184. <https://doi.org/10.1002/mas.20118>
- Neuman, J. A., Trainer, M., Brown, S. S., Min, K.-E., Nowak, J. B., Parrish, D. D., et al. (2016). HONO emission and production determined from airborne measurements over the Southeast U.S. *Journal of Geophysical Research: Atmospheres*, *121*, 9237–9250. <https://doi.org/10.1002/2016JD025197>
- Patton, E. G., Sullivan, P. P., & Moeng, C.-H. (2005). The influence of idealized heterogeneity on wet and dry planetary boundary layers coupled to the land surface. *Journal of the Atmospheric Sciences*, *62*(7), 2078–2097. <https://doi.org/10.1175/JAS3465.1>
- Ryerson, T., Williams, E., & Fehsenfeld, F. (2000). An efficient photolysis system for fast-response NO<sub>2</sub> measurements. *Journal of Geophysical Research*, *105*(D21), 26447–26461. <https://doi.org/10.1029/2000JD900389>
- Schwarz, J. P., Gao, R. S., Fahey, D. W., Thomson, D. S., Watts, L. A., Wilson, J. C., et al. (2006). Single-particle measurements of midlatitude black carbon and light-scattering aerosols from the boundary layer to the lower stratosphere. *Journal of Geophysical Research*, *111*(D16), D16207. <https://doi.org/10.1029/2006JD007076>
- Shetter, R. E., & Müller, M. (1999). Photolysis frequency measurements using actinic flux spectroradiometry during the PEM-Tropics mission: Instrumentation description and some results. *Journal of Geophysical Research*, *104*(D5), 5647–5661. <https://doi.org/10.1029/98JD01381>
- Veres, P. R., Neuman, J. A., Bertram, T. H., Assaf, E., Wolfe, G. M., Williamson, C. J., et al. (2020). Global airborne sampling reveals a previously unobserved dimethyl sulfide oxidation mechanism in the marine atmosphere. *Proceedings of the National Academy of Sciences of the United States of America*, *117*(9), 4505–4510. <https://doi.org/10.1073/pnas.1919344117>
- Wang, S., Hornbrook, R. S., Hills, A., Emmons, L. K., Tilmes, S., Lamarque, J.-F., et al. (2019). Atmospheric acetaldehyde: Importance of air-sea exchange and a missing source in the remote troposphere. *Geophysical Research Letters*, *46*, 5601–5613. <https://doi.org/10.1029/2019GL082034>
- Warner, J. X., Wei, Z., Strow, L. L., Barnett, C. D., Sparling, L. C., Diskin, G., & Sachse, G. (2010). Improved agreement of AIRS tropospheric carbon monoxide products with other EOS sensors using optimal estimation retrievals. *Atmospheric Chemistry and Physics*, *10*(19), 9521–9533. <https://doi.org/10.5194/acp-10-9521-2010>



- Weibring, P., Richter, D., Fried, A., Walega, J. G., & Dyroff, C. (2006). Ultra-high-precision mid-IR spectrometer II: System description and spectroscopic performance. *Applied Physics B*, *85*(2), 207–218. <https://doi.org/10.1007/s00340-006-2300-4>
- Weibring, P., Richter, D., Walega, J. G., & Fried, A. (2007). First demonstration of a high performance difference frequency spectrometer on airborne platforms. *Optics Express*, *15*(21), 13476–13495. <https://doi.org/10.1364/OE.15.013476>
- Yuan, B., Koss, A., Warneke, C., Gilman, J. B., Lerner, B. M., Stark, H., & de Gouw, J. A. (2016). A high-resolution time-of-flight chemical ionization mass spectrometer utilizing hydronium ions (H<sub>3</sub>O<sup>+</sup> ToF-CIMS) for measurements of volatile organic compounds in the atmosphere. *Atmospheric Measurement Techniques*, *9*(6), 2735–2752. <https://doi.org/10.5194/amt-9-2735-2016>